Constitutively active STING causes neuroinflammation and degeneration of dopaminergic neurons in mice

Eva M Szegö[1*], Laura Malz[2*], Nadine Bernhardt[3], Angela Rösen-Wolff[4], Björn H. Falkenburger[5#], Hella Luksch[6#]

[1]Department of Neurology, TU Dresden, Dresden, Germany; e-mail: Eva.Szego@uniklinikum-dresden.de

[2]Departments of Neurology & Pediatrics, TU Dresden, Dresden, Germany; e-mail: Laura.Malz@uniklinikum-dresden.de

[3]Department of Psychiatry, TU Dresden, Dresden, Germany; e-mail: Nadine.Bernhardt@uniklinikum-dresden.de

[4]Department of Pediatrics, TU Dresden, Dresden, Germany; e-mail: Angela.Roesen-Wolff@uniklinikum-dresden.de

[5]Department of Neurology, TU Dresden, Dresden, Germany; Deutsches Zentrum für Neurodegenerative Erkrankungen, Dresden, Germany; e-mail: bfalken@ukdd.de

[6]Department of Pediatrics, TU Dresden, Dresden, Germany; e-mail: Hella.Luksch@uniklinikum-dresden.de

* EMSz and LM contributed equally

# BHF and HL contributed equally

Abstract

The innate immune system can protect against certain aspects of neurodegenerative diseases, but also contribute to disease progression. Stimulator of interferon genes (STING) is activated after detection of cytoplasmic dsDNA by cGAS (cyclic GMP-AMP synthase) as part of the defense against viral pathogens, activating type I interferon and NF-kB/inflammasome signaling. In order to specifically test the relevance of this pathway for the degeneration of dopaminergic neurons in Parkinson's disease, we studied a mouse model with heterozygous expression of the constitutively active STING variant N153S.

In adult mice expressing N153S STING, the number of dopaminergic neurons was smaller than in controls, as was the density of dopaminergic axon terminals and the concentration of dopamine in the striatum. We also observed alpha-synuclein pathology and a lower density of synaptic puncta. Neuroinflammation was quantified by staining astroglia and microglia, by measuring mRNAs, proteins and nuclear translocation of transcription factors. Neuroinflammatory markers were already elevated in juvenile mice, thus preceding the degeneration of dopaminergic neurons. Inflammation and neurodegeneration were blunted in mice deficient for signaling by type I interferons or inflammasomes, but not suppressed completely.

Collectively, these findings demonstrate that chronic activation of the STING innate immunity pathway is sufficient to cause degeneration of dopaminergic neurons. This pathway could be targeted therapeutically.

Introduction

Inflammation contributes significantly to the pathogenesis of neurodegenerative diseases, including Parkinson's disease (PD) (Harms et al., 2021; Hirsch and Standaert, 2021). Inflammatory serum markers are associated with more severe PD symptoms and with a more rapid progression of cognitive decline (Hall et al., 2018; Mollenhauer et al., 2019). Anti-inflammatory drugs like aspirin have been associated with a lower risk of developing PD in epidemiological studies (Chen et al., 2003). The pathological hallmarks of PD include the degeneration of dopaminergic neurons in the substantia nigra and the cytoplasmic inclusions termed Lewy bodies (Obeso et al., 2017). Aggregates of alpha-synuclein (aSyn), one of the main constituents of Lewy bodies, stimulate monocytes and microglia (Grozdanov et al., 2019) and astroglia (Chou et al., 2021), suggesting that inflammatory changes in PD respond to aSyn pathology and contribute to disease progression (Harms et al., 2021; Hirsch and Standaert, 2021).

The stimulator of interferon genes (STING) responds to cytoplasmic dsDNA as part of the innate immunity defense against viral pathogens (Paul et al., 2021). STING is activated by cyclic GMP-AMP synthase (cGAS), which binds dsDNA and catalyzes synthesis of the second messenger cyclic GMP-AMP (Motwani et al., 2019). This pathway can be activated by viral nucleic acids but also by self-DNA (Chen et al., 2016; Li and Chen, 2018; Motwani et al., 2019). The cGAS-STING pathway has been implicated in the pathogenesis of PD (Beyer et al., 2020), but also Alzheimer's disease and amyotrophic lateral sclerosis (Chen et al., 2021; Li et al., 2021; Paul et al., 2021). For instance, mice deficient for the PD-associated proteins PINK and parkin fail to degrade damaged mitochondria, accumulate mitochondrial DNA in the cytosol and show a STING-mediated inflammatory phenotype after exhaustive exercise (Sliter et al., 2018).

The two main transcription factors activated by STING are the interferon regulatory factor 3 (IRF3) (Chen et al., 2021) and nuclear factor 'kappa-light-chain-enhancer' of activated B-cells (NF-κB) (Liu et al., 2014). Consequently, type I interferons (IFN) and pro-inflammatory cytokines are produced, triggering a secondary inflammation through the activation of inflammasomes (Hopfner and Hornung, 2020). Additionally, STING can activate inflammasomes directly (Wang et al., 2020). Inflammasomes are major signaling hubs that activate caspase-1 and control the bioactivity of pro-inflammatory cytokines of the interleukin (IL)-1 family (Gaidt et al., 2017; Schroder and Tschopp, 2010). Activation of inflammasomes formed by the NOD-, LRR- and pyrin domain-containing protein 3 (NLRP3)

has been linked to the progression of several neurodegenerative diseases (Heneka et al., 2018). NLRP3 immunoreactivity is increased in mesencephalic neurons of PD patients and NLRP3 variants are associated with the risk to develop PD (von Herrmann et al., 2018). Conversely, inhibiting NLRP3 mitigates degeneration of dopaminergic neurons and aSyn pathology in mouse models (Gordon et al., 2018). NRLP3 has also been associated with Alzheimer's disease (Heneka et al., 2018), prion disease (Nazmi et al., 2019), and traumatic brain injury (Sen et al., 2020).

Neuroinflammation receives growing attention in neurodegenerative diseases because it represents a promising therapeutic target. Designing such therapies requires, however, to determine the specific effects of individual components of this highly interconnected signaling network, which responds to diverse stimuli and involves many different cell types. Given the role of the STING pathway in PINK/parkin related damage (Sliter et al., 2018), we wanted to learn more about the role of STING for PD pathogenesis and determine whether specific activation of STING is sufficient to cause degeneration of dopaminergic neurons. In order to test this, we used a mouse model with heterozygous expression of the STING genetic variant N153S (Luksch et al., 2019). Constitutively active STING mutants cause an autoinflammatory disease in humans termed STING-associated vasculopathy with onset in infancy (SAVI) (Crow and Casanova, 2014; Liu et al., 2014). SAVI is characterized by systemic inflammation with acral vasculitis, T cell lymphopenia, and interstitial pulmonary disease. Major features of systemic inflammation in SAVI are recapitulated in STING N153S knockin mice (Luksch et al., 2019, Siedel et al., 2020). For simplicity, we refer to these as STING ki mice here and use the term STING WT for the corresponding wild type littermate controls. In this work, we determined the extent of neuroinflammation in the brains of young and adult mice, the extent of dopamine neuron degeneration, and aSyn pathology. Furthermore, we used additional knockout mice to determine which of the known downstream signaling pathways contribute to STING-induced neurodegeneration.

101 ## Materials and Methods

102 Source of chemicals, antibodies, composition of buffers, equipment and software used in this
103 study are listed in supplemental Table S1.
104

105 **Animals**

106 All animal experiments were carried out in accordance with the European Communities
107 Council Directive of November 24, 1986 (86/609/EEC) and approved by the Landesdirektion
108 Dresden, Germany. Mice of both sexes were housed under a 12-hour light and dark cycle
109 with free access to pelleted food and tap water in the Experimental Center, Technische
110 Universität, Dresden, Germany. Heterozygous STING N153S/WT ki mice (STING ki) were
111 previously described (Luksch et al., 2019). STING ki or STING WT mice were crossed to
112 *Ifnar1*$^{-/-}$ mice (a gift from Axel Roers, Dresden, Germany) and *Casp1*$^{-/-}$ mice (a gift from
113 Stefan Winkler, Dresden, Germany).

114 For all genotypes, five-week-old (from here referred as juvenile) or 20-23-week-old
115 (referred as adult) animals were sacrificed with an overdose of isoflurane (Baxter, Lessines,
116 Belgium). For western blot analysis and for gene expression analysis, brains were rapidly
117 removed from the skull and washed in ice-cold Tris-buffered saline (TBS, pH 7.4). Cortex
118 and striatum were dissected, snap-frozen in liquid nitrogen and stored at -80°C until use. For
119 histology, mice were perfused transcardially with 4 % paraformaldehyde (PFA) in TBS. After
120 post-fixation (4 % PFA, overnight) and cryoprotection (30 % sucrose in TBS), 30 µm-thick
121 coronal brain sections were cut in a cryostat (Leica, Germany).
122

123 **Immunofluorescence stainings of mouse brain sections**

124 To quantify the number of dopaminergic neurons in the *substantia nigra* (SN), every fifth
125 section throughout the entire SN was stained for tyrosine hydroxylase (TH) as previously
126 (Szegő et al., 2021). In brief, after blocking (2 % bovine serum albumin, 0,3 % Triton X-100
127 in TBS; 1 h RT), sections were incubated with the primary antibody in blocking solution (two
128 overnights), followed by the fluorescently labelled secondary antibody (Alexa 488
129 conjugated donkey anti-sheep, 1:2000, overnight). Sections were counterstained with Hoechst
130 and mounted with Fluoromount-G.

131 To quantify the density of dopaminergic axon terminals (fibers) and neuroinflammation
132 in the striatum, every sixth section throughout the entire striatum was stained with a cocktail
133 of primary antibodies: TH (Pel Freeze, P40101, 1:1000), Iba1 (Wako, 019-19741, 1:1000)

134 and GFAP (abcam, ab4674, 1:2000). As fluorescently labelled secondary antibodies, Alexa
135 488 conjugated donkey anti-sheep, Alexa 555 conjugated donkey anti-rabbit, Alexa 647
136 conjugated donkey anti-chicken were used (1:2000, overnight). Sections were counterstained
137 with Hoechst and mounted with Fluoromount-G.
138
139 **Quantification of dopaminergic neuron number, striatal fiber density and gliosis**
140 The number of dopaminergic somata in the SN was determined by supervised manual
141 counting by an investigator blinded to the experimental groups. For each animal, every fifth
142 section throughout the rostro-caudal extent of the SN (2.54 to -3.88 mm posterior to Bregma
143 based on Paxinos and Franklin, 2001) was incorporated into the counting procedure. In each
144 section, z stacks were acquired (step size: 2 µm, 5 slices in total) from both hemispheres with
145 a 20x objective (N.A 0.8, Axio Imager 2, Zeiss). Stacks were stitched to reconstruct the entire
146 SN. After adjusting the threshold and carefully marking the borders of the SN, only TH-
147 positive cell bodies with a visible nucleus in the blue channel were counted by ImageJ (1,53c;
148 Cell Counter plugin).The total number of neurons per SN was estimated by multiplying the
149 counted cell number by five (every fifth section was used for this analysis). For quantification
150 of gliosis, five fluorescent images were acquired from every sixth striatal section stained for
151 GFAP and Iba1 using a 20x objective. After adjusting the threshold and noise removal
152 (Background subtraction, rolling ball radius 50) from the individual images (separately for
153 GFAP and Iba1 channels), the area fraction was determined by ImageJ from ten regions of
154 interest per image. Results were analyzed using a generalized linear mixed model (glm) in
155 RStudio with a hierarchically nested design (expressed as percent area) as previously (Szegő
156 et al., 2021).
157 From the same striatal sections, the density of the dopaminergic axon terminals (fibers)
158 was determined as described previously (Szegő et al., 2012). In brief, z-stack images were
159 acquired (five planes, 0.5 µm step size, 100x objective, N.A. 1.4; Axio Imager 2, Zeiss). TH-
160 positive fibers were delineated from the maximal intensity projection (ImageJ) after adjusting
161 the threshold, noise removal and binarization, and density was expressed as percent area.
162 Every sixth section per animal, five images per section and ten boxes per image were
163 analyzed in a hierarchically nested design as above.
164
165 **Protein analyses**
166 To detect protein changes, cortical and striatal tissue were mechanically lysed in a buffer
167 containing 250 mM sucrose, 50 mM TRIS (pH 7,5), 1 mM EDTA, 5 mM $MgCl_2$, 1 % Triton

168 X-100 in the presence of protease and phosphatase inhibitors (MedChem Express) as
169 previously (Szegő et al., 2012). Samples were centrifuged (14000 g, 30 min, 4 °C) and
170 protein concentration in the supernatant was determined with the BCA method
171 (ThermoFisher, Germany). After boiling with 4x Laemmli buffer (1 M Tris pH 6.8, 0.8 %
172 SDS, 40 % glycerol, 5 % β-mercaptoethanol, traces of bromophenol blue, 5 min, 95 ºC), 5 µg
173 protein was loaded onto a 4-20 % Tris/glycine SDS gel for western blot analysis. Membranes
174 were fixed in paraformaldehyde (10 min, RT) and blocked with 1 % bovine serum albumin,
175 0,05 % Tween 20 in TBS. Membranes were incubated first in the presence of antibodies
176 against phosphorylated aSyn and aSyn, (Cell Signaling), then with βIII-tubulin as loading
177 control (overnight, 4 ºC). Following washing, membranes were incubated in the presence of
178 horseradish peroxidase-conjugated secondary antibodies (donkey anti-mouse or donkey anti-
179 rabbit). Signal was detected using chemiluminescent substrate and a camera-based system.
180 ImageJ was used to determine the optical density of protein bands and all data were analyzed
181 for each group (n = 5 animals/group) based on 3 independent blots. Optical densities were
182 normalized to the expression of the density of the tubulin loading control of the same sample,
183 and then expressed relative to the WT animals.
184
185 **Gene expression analyses**
186 Total RNA was extracted from snap frozen dissected prefrontal cortex tissue by using the
187 RNeasy Mini Kit (Qiagen, Germany) according to the manufacturer's instructions. cDNA
188 was generated by MMLV reverse transcription (Promega Germany). Quantitative Real Time
189 PCR assays were carried out by using QuantStudio 5 (Thermo Fisher Scientific, Germany)
190 and GoTaq®aPCR Master Mix with SYBR green fluorescence (Promega, Germany). PCR
191 primer sequences were retrieved from the Primer Bank database (Spandidos et al., 2009).
192 Expression of genes was normalized to the expression of the housekeeping genes (*Hprt1*,
193 *Rpl13a*, *Eef2*) and to the STING WT by using the ΔΔCt method. Sequences of primers are
194 listed in supplemental Table S2.
195
196 **Statistical analyses**
197 Sample numbers for each analysis are listed in supplemental Table S4. In graphs, markers
198 represent individual animals; lines represent mean and standard deviation (SD) of all animals.
199 Data normality was tested by the Kolmogorov-Smirnov test and graphically by QQ plot (R,
200 version 2.8.0; R Development Core Team 2008). Grubbs test was used to identify outliers. t-
201 test, Mann-Whitney test or two-way ANOVA were performed using GraphPad Prism

(Versions 5.01 and 9.0.0). Linear regression was performed using R. For generalized linear mixed-effects model (Szegő et al., 2021), animal, section and image were used as random effects nested within each other (R package: lme4). p values are indicated in the graphs by symbols with * representing $p<0.05$, ** representing $p<0.01$, *** representing $p<0.001$. Exact p values are given in the Figure legends.

207 **Results**

208 **Neuroinflammation and degeneration of dopaminergic neurons in mice with**
209 **constitutive STING activation**

210 To characterize the neuronal phenotype in adult STING ki mice, we assessed
211 neuroinflammation and the integrity of the dopaminergic nigrostriatal system. First, we
212 stained striatal sections for Iba1 to determine the activation of microglia. The Iba1 positive
213 area fraction was 9-fold higher in STING ki mice than in STING WT (Figure 1A and E).
214 Activation of astroglia, as determined by GFAP staining, was 26-fold higher in STING ki
215 mice than in STING WT (Figure 1B and F). Thus, STING ki mice exhibit a strong
216 neuroinflammatory phenotype, consistent with increased systemic inflammation (Luksch et
217 al., 2019).

218 Next, we asked whether the chronic neuroinflammation in the STING ki mice is
219 associated with the degeneration of dopaminergic neurons. Somata of dopaminergic neurons
220 in the *substantia nigra* (SN, Figure 1C) and dopaminergic axon terminals in the striatum
221 (Figure 1D) were identified by staining for tyrosine hydroxylase (TH). The SN of STING ki
222 mice contained significantly fewer TH-positive neurons than the SN of STING WT (Figure
223 1G and figure supplement 1A). Similarly, the density of dopaminergic axon terminals (fibers)
224 in the striatum was lower in STING ki mice than in STING WT (Figure 1H). Accordingly,
225 the concentration of dopamine in the striatum was lower in STING ki mice than in STING
226 WT mice (Figure 1I). The concentration of dopamine metabolites was higher in STING ki
227 mice (supplemental Figure 1B), suggesting increased dopamine turnover as commonly
228 observed with dopamine depletion. Taken together, these findings demonstrate that the
229 integrity of nigrostriatal dopaminergic neurons is compromised in STING ki mice.

230

231 **Neuroinflammation without obvious degeneration of the dopaminergic neurons in**
232 **juvenile mice with constitutive STING activation**

233 In order to explore whether the compromised integrity of dopaminergic neurons is a
234 consequence of a prolonged neuroinflammation, we next analyzed brain sections of juvenile
235 (5-week-old) STING ki and STING WT mice (Figure 2). Microglia was already significantly
236 activated in juvenile STING ki mice. The area fraction of the Iba1 staining was 2-fold higher
237 in STING ki mice than in STING WT (Figure 2A and E). Similarly, the area fraction of
238 GFAP signal was 14-fold higher in STING ki mice than in STING WT (Figure 2B and F),
239 suggesting activation of astroglia in juvenile STING ki mice. However, the number of TH-

positive neurons in the *substantia nigra* was not different between juvenile STING ki mice and STING WT (Figure 2C and G, figure supplement 1C). Similarly, striatal axon terminals (Figure 2D and H) and the concentrations of striatal dopamine and its metabolites (Figure 2I, figure supplement 1D) were not different between STING ki mice and STING WT.

Taken together, these findings demonstrate that the compromised integrity of the nigrostriatal system in adult STING ki mice (Figure 1) represents an adult-onset neurodegeneration and not a developmental defect. Given that activation of microglia and astroglia in STING ki mice precedes degeneration of dopaminergic neurons, STING-induced neuroinflammation could contribute to the neurodegeneration.

aSyn pathology and synaptic defects in the striatum of STING ki mice

To analyze aSyn pathology in the striatum of STING ki mice, we measured the amount of aSyn protein phosphorylated at serine 129 (paSyn), which is considered one of the major pathological forms of aSyn (Anderson et al., 2006; Fujiwara et al., 2002; Samuel et al., 2016). Lysates of adult STING ki mice contained a substantial amount of paSyn (Figure 3A), which was barely detectable in STING WT. The amount of total aSyn was lower in STING ki mice (Figure 3C) and the ratio of paSyn to total aSyn increased (Figure 3D) – as commonly observed in synucleinopathy models and PD patients (Anderson et al., 2006; Chatterjee et al., 2020; Fujiwara et al., 2002; Szegö et al., 2022).

Thioflavin S (ThioS) binds to the characteristic β-sheet conformation of amyloid-containing proteins, including aSyn (Froula et al., 2019; Neumann et al., 2002). The number of cells with ThioS-positive inclusions was higher in the striatum of adult STING ki mice than in STING WT (Figure 3 B and E), consistent with the findings from the aSyn immunoblots.

Since dopamine depletion and aSyn pathology can compromise synaptic integrity, we next quantified the density of synapses in the striatum. Presynaptic puncta were detected by staining against synapsin; post-synaptic puncta were detected by staining against homer (Figure 3F and G). The density of synapsin puncta was 18% lower in adult STING ki than in STING WT (Figure 3H), the density of post-synaptic puncta was 9% lower in STING ki than in STING WT mice (Figure 3I). In summary, we observed aSyn pathology and a reduced density of synapses in the striatum of adult STING ki mice.

Type I IFN signaling and NF-κB/inflammasome dependent signaling are activated in the brain of STING ki mice

In order to analyze the signaling pathways by which constitutively active STING causes degradation of dopaminergic neurons and aSyn pathology, we examined the expression of selected interferon-stimulated genes (ISGs) by quantitative real time PCR in juvenile and adult STING ki and STING WT mice (Figure 4A-D). In STING WT mice, we observed an age-dependent increase for interferon-induced GTP-binding protein Mx1 (*Mx-1*, 10-fold, p= 0,0000006, comparison not depicted in Figure 4. for clarity), interferon-gamma induced protein 10 kD (*Ip-10*, 22-fold, p= 0,000105) and *Sting1* (3,7-fold, p=0,0008399), consistent with previous findings (Harris et al., 2020).

In STING ki mice, the expression of ISGs was generally higher than in STING WT, both comparing juvenile mice and comparing adult mice (Figures 4A-D, p-values in Figure legend). The expression of *Sting1* was not significantly different between adult STING ki and STING WT, confirming that the expression of the STING N153S mutant is not changing.

cGAS/STING activation also leads to the activation of NF-κB/inflammasome pathway (Balka et al., 2020; Balka and De Nardo, 2021; Wang et al., 2020). We therefore analyzed induction of the NF-κB/inflammasome pathway by quantitative real time PCR of the downstream mediators, tumor necrosis factor alpha (*Tnfα*), interleukin 1 beta (*Il-1β*), and caspase 1 (*Casp1*) (Figure 4E-G). In STING WT mice, the expression of *Tnfα*, *Il-1β*, *Casp1* increased with age (*Tnfα*: 5-fold, p= 0,0238678; *Il-1β*: 21-fold, p= 0,0000038; *Casp1*: 150-fold, p<0,00001, comparisons not depicted in Figure 4. for clarity), consistent with earlier reports (Mejias et al., 2018). In juvenile STING ki mice, the expression of *Tnfα* was 13-fold higher than in juvenile STING WT (Figure 4E; p= 0,0001448), *Il-1β* was 33-fold higher (Figure 4F, p= 0,00005) and *Casp1* was 9-fold higher (Figure 4G; p= 0,0000369). In adult mice, expression of *Tnfa* and *Casp1* was not different between STING WT and STING ki whereas expression of *Il-1β* was 6-fold higher in adult STING ki than in adult STING WT (Figure 4F, p= 0,0389).

STAT3 and NF-κB translocate to the nucleus in STING ki mice

Nuclear trafficking is critical for the function of transcription factors such as STAT3 and NF-κB (Balka and De Nardo, 2021; Noguchi et al., 2013). To further investigate the activation of the type I IFN and NF-kB-dependent pathways in juvenile and adult STING ki mice, we quantified the number of nuclei positive for phosphorylated STAT3 (pSTAT3) and NF-κB in the striatum (Figure 5). There were only very few pSTAT3-positive nuclei in juvenile and

307 adult STING WT mice (Figure 5A and C). In juvenile STING ki mice, the average number of
308 pSTAT3-positive nuclei was 4-fold higher than in juvenile STING WT mice (Figure 5C, p=
309 0,05678, 2-way ANOVA). In adult STING ki mice, the number of pSTAT3-positive nuclei
310 was 15-fold higher than in STING WT (p= 0,00004). Similarly, the number of NF-kB-
311 positive nuclei was 3-fold higher in juvenile STING ki mice than in STING WT (Figure 5B
312 and, p= 0,009). In adult STING ki mice, the number of NF-kB-positive nuclei was 6-fold
313 higher than in STING WT (Figure 5D, p= 0,007).
314 Taken together, our results show nuclear translocation of pSTAT3 and NF-kB in the
315 striatum of STING ki mice, consistent with a robust activation of type I IFN and NF-
316 kB/inflammasome dependent signaling in STING ki mice.
317
318 **Type I IFN and NF-kB/inflammasome signaling contribute to neuroinflammation in**
319 **STING ki mice**
320 We next sought to investigate the contribution of the type I IFN and NF-kB/inflammasome
321 signaling pathways to neuroinflammation in STING ki mice. In order to test the involvement
322 of the IFN dependent pathway, we crossed STING ki mice with mice deficient for type I IFN
323 receptor (*Ifnar1*$^{-/-}$); in order to test the involvement of the NF-kB/inflammasome pathway, we
324 crossed STING ki mice with mice deficient for caspase-1 (*Casp1*$^{-/-}$).
325 We first analyzed ISGs and NF-kB dependent gene expression by quantitative real time
326 PCR in adult *Ifnar1*$^{-/-}$ and *Casp1*$^{-/-}$ mice (Figure 6A-E). The N153S STING-induced increase
327 in the interferon dependent genes *Ifi44 and Mx-1* was abrogated in *Ifnar1*$^{-/-}$ mice (Figure 6A
328 and B), but unaltered in *Casp1*$^{-/-}$ mice. This is consistent with the dependence of *Ifi44 and*
329 *Mx-1* on type I interferon signaling. The N153S STING-induced increase in expression of *Il-*
330 *1*β (Figure 6C) was abrogated in *Casp1*$^{-/-}$ mice, but not in *Ifnar1*$^{-/-}$ mice, consistent with the
331 fact that *Il-1*β is NF-κB dependent. The N153S STING-induced increase in *Ip-10* expression
332 was 17-fold in WT (Figure 6D, p= 0,0030844), 12-fold in *Ifnar1*$^{-/-}$ (p= 0,002589) and 6-fold
333 in *Casp 1*$^{-/-}$ (p= 0,0041598), i.e. not statistically different between WT and *Ifnar1*$^{-/-}$ mice (p=
334 0,4398) or *Casp 1*$^{-/-}$ mice (p= 0,0623). Expression of *Tnfa* (Figure 6E) was not different
335 between STING ki and STING WT in this age group, consistent with Figure 5A, and
336 unaltered in *Ifnar1*$^{-/-}$ and *Casp1*$^{-/-}$ mice. Expression of *Sting1* was also not altered in any on
337 the genotypes (figure supplement 2A), confirming that alteration in transgene expression did
338 not underlie the observed effects. Collectively, these analyses confirm the activation of both
339 IFN signaling and NF-κB/inflammasome signaling in the brain of STING ki mice. *Ifnar1*$^{-/-}$

340 selectively interferes with the interferon dependent pathway whereas *Casp1*$^{-/-}$ interferes with
341 the NF-kB/inflammasome pathway.
342 We next measured glial activation in *Ifnar1*$^{-/-}$ and *Casp1*$^{-/-}$ mice. N153S STING-
343 induced activation of microglia was still observed in adult *Ifnar1*$^{-/-}$ and *Casp1*$^{-/-}$ mice (Figure
344 6F and H, fold increase and p values in legend). In order to determine whether the extent of
345 N153S STING-induced microglia activation was significantly different between *Ifnar1*$^{-/-}$
346 mice and Ctrl., we calculated the interaction between the factors 'STING genotype' and
347 '*Ifnar1* genotype' in two-way ANOVA. The extent of microglia activation was significantly
348 smaller in adult *Ifnar1*$^{-/-}$ mice (p= 0,004724) than in Ctrl. Similarly, the extent of N153S
349 STING-induced microglia activation was significantly smaller in *Casp1*$^{-/-}$ mice (p=
350 0,000021). The extent of N153S STING-induced microglia activation did not differ between
351 *Ifnar1*$^{-/-}$ and *Casp1*$^{-/-}$ (p= 0,0805731). Collectively, these findings suggest that N153S
352 STING-induced microglia activation depends both on type 1 IFN signaling and on NF-
353 kB/inflammasome signaling.
354 The extent of N153S STING-induced astroglia activation (Figure 6G and I) was
355 significantly reduced from 26-fold in Ctrl. to 16-fold in *Ifnar1*$^{-/-}$ (p=0,0158378 for interaction
356 of 2-way ANOVA) and to 4-fold in *Casp1*$^{-/-}$ (p<0.00001 for interaction of 2-way ANOVA),
357 suggesting that astroglia activation might depend more on NF-kB/inflammasome signaling
358 than on interferon dependent signaling.
359
360 **Type I IFN and NF-kB/inflammasome signaling contribute to neurodegeneration in**
361 **STING ki mice**
362 Next, we asked whether the N153S STING-induced degeneration of dopaminergic axon
363 terminals in the striatum is abrogated in adult *Ifnar1*$^{-/-}$ and *Casp 1*$^{-/-}$ mice (Figure 7).
364 Interestingly, the density of dopaminergic axon terminals in the striatum was already lower in
365 *Ifnar1*$^{-/-}$ mice and *Casp 1*$^{-/-}$ mice with WT STING than in control *Ifnar1*$^{+/+}$ and *Casp1*$^{+/+}$ mice
366 (p= 0,0143071 and p= 0,0000248, two-way ANOVA). These findings suggest that *Ifnar1* and
367 *Casp1* are required for proper proliferation, maturation and/or maintenance of dopaminergic
368 neurons and their axon terminals. Indeed, the Wnt-β-catenin pathway is regulated by
369 interferons (Kovács et al., 2019) and regulates the differentiation of midbrain dopaminergic
370 neurons (Szegő et al., 2017). Furthermore, IL-1β induces the differentiation of dopaminergic
371 neurons (Ling et al., 1998; Rodriguez-Pallares et al., 2005), and we found marginally reduced
372 *Il-1b* expression in adult *Casp1*$^{-/-}$ mice (Figure 6C STING WT).

373 Both in *Ifnar1*$^{-/-}$ and in *Casp 1*$^{-/-}$ mice, the N153S STING-induced degeneration of
374 dopaminergic axon terminals in the striatum was less pronounced than in the control
375 *Ifnar1*$^{+/+-}$ and *Casp1*$^{+/+}$ mice (p= 0,00157 and p= 0,007326 for interaction in two-way
376 ANOVA). N153S STING-induced fiber loss was not statistically different between *Ifnar1*$^{-/-}$
377 and *Casp1*$^{-/-}$ mice (p= 0,468 for interaction). Consistent with the less pronounced
378 degeneration of dopaminergic axon terminals, the N153S STING-induced reduction in
379 striatal dopamine and increase in its metabolism was not observed in *Ifnar1*$^{-/-}$ and *Casp1*$^{-/-}$
380 mice (Figure 7C, figure supplement 2B). These findings suggest that both pathways
381 contribute to the degeneration of dopaminergic axon terminals, and blocking either pathway
382 could reduce neurodegeneration.

383 **Discussion**

384 In this work, we demonstrated that the expression of the constitutively active STING variant
385 N153S causes neuroinflammation, followed by degeneration of dopaminergic neurons and
386 aSyn pathology. N153S STING-induced microglia activation and degeneration of
387 dopaminergic neurons involve both type I IFN-dependent and NF-κB/inflammasome-
388 dependend signaling, while astroglia activation might depend predominantly on the NF-
389 κB/inflammasome pathway.

390

391 **Constitutive STING activation causes neuroinflammation**

392 STING is expressed in the central nervous system. Its expression is highest in microglia, but
393 it can also be detected in astroglia and neurons (Jeffries and Marriott, 2017). Microglia are
394 the primary immune cells of the central nervous system (Wolf et al., 2017) and highly
395 activated upon pathogen invasion or tissue damage. Microglia activation in STING ki mice
396 (Figure 1 and 2) is therefore in line with the increased inflammatory phenotype found in the
397 lungs and spleen of STING ki mice (Luksch et al., 2019; Siedel et al., 2020) and in patients
398 with STING-associated vasculopathy with onset in infancy syndrome (Liu et al. 2014).

399 Consistent with this morphologically defined neuroinflammatory phenotype, we
400 observed increased expression of the ISGs *Ifi44* and *Mx-1* (Figure 4). These effects are
401 associated with interferon signaling, the main pathway downstream of STING (Decout et al.,
402 2021), demonstrating that expressing the N153S mutant of STING indeed activates interferon
403 dependent pathways. Microglia activation was reduced when N153S STING was expressed
404 in mice deficient for Ifnar1 (*Ifnar1*$^{-/-}$, Figure 6H), confirming that the type I IFN pathway is
405 involved in STING-dependent microglia activation as previously demonstrated by others
406 (Warner et al., 2017). However, microglia activation by N153S STING was not completely
407 blocked in *Ifnar1*$^{-/-}$ mice, suggesting that additional pathways are involved.

408 Indeed, next to type I IFN signaling, we also observed increased expression of *Il-1b*
409 and *Tnfa* (Figure 4), confirming the activation of the NF-κB/inflammasome pathway in
410 STING ki mice (Balka et al., 2020; Balka and De Nardo, 2021; B. C. Liu et al., 2018).
411 Consistently, in STING ki mice, nuclear translocation of NF-κB was observed significantly
412 more often (Figure 5). We also observed increased expression of *Casp1*, indicating that the
413 inflammasome pathways are activated by constitutively active STING, consistent with
414 previous work about systemic inflammation (Luksch et al., 2019). Accordingly, the extent of
415 microglia activation by N153S STING was reduced in *Casp1*$^{-/-}$ mice (Figure 6H). Therefore,

416 our results suggest that STING-dependent microglia activation involves inflammasome
417 activation, in addition to type I IFN-dependent pathways.
418 Next to the activation of microglia, we also observed activation of astroglia (Figures 1
419 and 2). STING-induced astroglia activation was only blunted in *Ifnar1*$^{-/-}$ mice, but it was
420 completely blocked in *Casp1*$^{-/-}$ mice (Figure 6I). This finding suggests that chronic STING-
421 induced astroglia activation might depend mainly on NF-κB/inflammasome signaling.
422 Astroglia activation can result directly from the expression of N153S STING in astroglia and
423 indirectly through the activation of microglia (Kwon and Koh, 2020; Wolf et al., 2017). The
424 differential effect in *Ifnar1*$^{-/-}$ and *Casp1*$^{-/-}$ mice suggests that astroglia activation is not only a
425 downstream consequence of microglia activation.
426
427 **Chronic STING activation leads to the degeneration of dopaminergic neurons**
428 We observed a reduced number of TH-positive neurons in the *substantia nigra* of STING ki
429 mice, a reduced density of dopaminergic axon terminals and a reduced concentration of
430 striatal dopamine (Figure 1G-I). These changes occurred in adult mice and were not present
431 in juvenile mice (Figure 2G-I). The degeneration of dopaminergic neurons thus is a
432 consequence of the inflammatory changes in our model.
433 On the *Ifnar1*$^{-/-}$ and *Casp1*$^{-/-}$ backgrounds, the effect of STING ki was difficult to
434 assess. Yet, the relative reduction in TH fiber density in STING ki mice, as compared to
435 STING WT mice, was smaller on the *Ifnar1*$^{-/-}$ and *Casp1*$^{-/-}$ backgrounds than in controls
436 (Figure 7B), as was the extent of dopamine depletion F (Figure 7C). These findings are
437 consistent with the partial rescue of microglia activation in *Ifnar1*$^{-/-}$ and *Casp1*$^{-/-}$ mice (Figure
438 6F and H). They suggest that both pathways contribute to the degeneration of dopaminergic
439 neurons. In further studies, the developmental effects of *Ifnar1* and *Casp1* deficiency could
440 be circumvented by using conditional knockout mice or pharmacological inhibitors.
441 In our model, degeneration of dopaminergic neurons and their axon terminals in STING
442 ki mice is likely a secondary effect of glia activation and secretion of inflammatory cytokines
443 – in line with previous findings demonstrating a role for inflammation in the pathogenesis of
444 PD (Hall et al., 2018; Mollenhauer et al., 2019). In addition, constant STING activity within
445 dopaminergic neurons could contribute to their degeneration – both in our STING ki mice
446 and in the pathogenesis of PD. Indeed, dopaminergic neurons accumulate oxidative damage
447 as a consequence of dopamine synthesis and electrical pacemaking activity (Guzman et al.,
448 2010), and even moderate oxidative stress can stimulate the STING pathway (Sliter et al.,

2018; West et al., 2015). Further work is required to determine the importance of STING activation in dopaminergic neurons for their degeneration in this model.

Accumulation of protein aggregates in STING ki mice

We observed an accumulation of pathological aSyn and an increased number of Thioflavin S positive cells in STING ki mice (Figure 3A-E). These findings suggest that chronic STING activation induces aSyn pathology. They are consistent with the recent observation that priming rats with a mimic of viral dsDNA precipitates aSyn pathology (Olsen et al., 2019) and with the aSyn aggregation following viral encephalitis (Bantle et al., 2021). Inflammatory signals are therefore active promotors of aSyn pathology and not only responsive to aSyn pathology.

The mechanism by which prolonged neuroinflammation leads to aSyn pathology is still unknown. Both inflammation and IFN induce the expression of the double-stranded (ds) RNA-dependent protein kinase (PKR) (Gal-Ben-Ari et al., 2019). PKR can phosphorylate aSyn at serine 129, resulting in aSyn pathology (Reimer et al., 2018). Moreover, clearance of aSyn aggregates occurs primarily through autophagy (Ebrahimi-Fakhari et al., 2011), and INFα increases expression of mammalian target of rapamycin (mTOR) (Liu et al., 2016), which is expected to reduce autophagy initiation. On the other hand, acute STING activation can induce autophagy (Hopfner and Hornung, 2020; Y. Liu et al., 2018; Moretti et al., 2017). aSyn pathology in our model therefore could be explained by an exhaustion of the autophagy machinery, as it was suggested recently (Bido et al., 2021), and the overall effect of inflammatory pathways on autophagy and aSyn pathology could be bimodal. Accordingly, degeneration of dopaminergic neurons and accumulation of aSyn aggregates was also observed in mice deficient for IFNβ (Ejlerskov et al., 2015; Magalhaes et al., 2021).

Conclusions

In this work, we observed the degeneration of dopaminergic neurons in mice expressing a constitutively active STING variant. These findings support the hypothesis that chronic neuroinflammation is sufficient to trigger degeneration of dopaminergic neurons and aSyn pathology. They indicate that neuroinflammation plays an active role in the pathogenesis of PD and could be a promising therapeutic target. Further work is required to determine the precise signaling pathway by which STING activation causes aSyn pathology and dopamine neuron degeneration.

482 **Declarations**

483 **Ethical Approval and Consent to participate**

484 Animals were approved by local authorities (Landesdirektion Dresden)and conducted in
485 accordance with guidelines of the Federation for European Laboratory Animal Science
486 Associations (FELASA).

487

488 **Consent for publication**

489 All authors approved the manuscript.

490

491 **Availability of data and materials**

492 The dataset supporting the conclusions of this article is included within the article and its
493 additional files.

494

495 **Competing interests**

496 The authors declare that they have no competing interests.

497

498 **Funding**

499 This work was supported by the German Research Foundation (DFG) SFB TRR237, B18 and
500 FA-658-3-1.

501

502 **Authors' contributions**

503 EMSz, ARW, BHF and HL conceived research. EMSz, LM, NB and HL performed research
504 and analyzed data. MG and MM provided human samples. EMSz, ARW, BHF and HL wrote
505 the first draft of the manuscript. All authors contributed and approved the manuscript.

506

507 **Acknowledgements**

508 We thank Min Ae Lee-Kirsch (TU Dresden) for very helpful comments on the manuscript
509 and Andrea Kempe, Annett Böhme, Katrin Höhne and Kristin Wogan for excellent technical
510 assistance.

511 **List of Abbreviations**

aSyn	alpha-synuclein
Casp1	Caspase1
cGAS	cyclic GMP-AMP synthase
dsDNA	double strand DNA
GFAP	glial fibrillary acidic protein
Iba1	ionized calcium-binding adapter molecule 1
Ifi44	interferon induced protein 44
IFN	interferon
Ifnar1	interferon alpha receptor1
Il-1β	interleukin 1 beta
Ip-10	interferon-gamma induced protein 10 kD
IRF3	interferon regulatory factor 3
ISG	interferon-stimulated gene
ki	knock in
Mx1	interferon-induced GTP-binding protein
NF-kB	nuclear factor 'kappa-light-chain-enhancer' of activated B-cells
NRLP3	the nucleotide-binding oligomerization domain (NOD), leucine-rich repeat (LRR)-containing protein 3
PD	Parkinson's disease
SAVI	STING-associated vasculopathy with onset in infancy
SN	substantia nigra
STAT3	signal transducer and activator of transcription 3
STING	stimulator of interferon genes
TH	tyrosine hydroxylase
TNFβ	tumor necrosis factor beta
WT	wild type

512

513 **References**

514 Anderson JP, Walker DE, Goldstein JM, De Laat R, Banducci K, Caccavello RJ, Barbour R,
515 Huang J, Kling K, Lee M, Diep L, Keim PS, Shen X, Chataway T, Schlossmacher MG,
516 Seubert P, Schenk D, Sinha S, Gai WP, Chilcote TJ. 2006. Phosphorylation of Ser-129
517 is the dominant pathological modification of α-synuclein in familial and sporadic lewy
518 body disease. *J Biol Chem* **281**:29739–29752. doi:10.1074/JBC.M600933200

519 Balka KR, De Nardo D. 2021. Molecular and spatial mechanisms governing STING
520 signalling. *FEBS J* **288**:5504–5529. doi:10.1111/FEBS.15640

521 Balka KR, Louis C, Saunders TL, Smith AM, Calleja DJ, D'Silva DB, Moghaddas F, Tailler
522 M, Lawlor KE, Zhan Y, Burns CJ, Wicks IP, Miner JJ, Kile BT, Masters SL, De Nardo
523 D. 2020. TBK1 and IKKε Act Redundantly to Mediate STING-Induced NF-κB
524 Responses in Myeloid Cells. *Cell Rep* **31**. doi:10.1016/J.CELREP.2020.03.056

525 Bantle CM, Rocha SM, French CT, Phillips AT, Tran K, Olson KE, Bass TA, Aboellail T,
526 Smeyne RJ, Tjalkens RB. 2021. Astrocyte inflammatory signaling mediates α-synuclein
527 aggregation and dopaminergic neuronal loss following viral encephalitis. *Exp Neurol*
528 **346**. doi:10.1016/j.expneurol.2021.113845

529 Beyer MMSS, Lonnemann N, Remus A, Latz E, Heneka MT, Korte M. 2020. Enduring
530 Changes in Neuronal Function upon Systemic Inflammation Are NLRP3 Inflammasome
531 Dependent. *J Neurosci* **40**:5480–5494. doi:10.1523/JNEUROSCI.0200-20.2020

532 Bido S, Muggeo S, Massimino L, Marzi MJ, Giannelli SG, Melacini E, Nannoni M, Gambarè
533 D, Bellini E, Ordazzo G, Rossi G, Maffezzini C, Iannelli A, Luoni M, Bagicaluppi M,
534 Gregori S, Nicassio F, Broccoli V. 2021. Microglia-specific overexpression of α-
535 synuclein leads to severe dopaminergic neurodegeneration by phagocytic exhaustion and
536 oxidative toxicity. *Nat Commun 2021 121* **12**:1–15. doi:10.1038/s41467-021-26519-x

537 Chatterjee K, Roy A, Banerjee R, Choudhury S, Mondal B, Halder S, Basu P, Shubham S,
538 Dey S, Kumar H. 2020. Inflammasome and α-synuclein in Parkinson's disease: A cross-
539 sectional study. *J Neuroimmunol* **338**. doi:10.1016/J.JNEUROIM.2019.577089

540 Chen H, Zhang SM, Hernán MA, Schwarzschild MA, Willett WC, Colditz GA, Speizer FE,
541 Ascherio A. 2003. Nonsteroidal Anti-inflammatory Drugs and the Risk of Parkinson
542 Disease. *Arch Neurol* **60**:1059. doi:10.1001/archneur.60.8.1059

543 Chen K, Lai C, Su Y, Bao WD, Yang LN, Xu P-P, Zhu L-Q. 2021. cGAS-STING-mediated
544 IFN-I response in host defense and neuro-inflammatory diseases. *Curr Neuropharmacol*
545 **19**. doi:10.2174/1570159X19666210924110144

546 Chen Q, Sun L, Chen ZJ. 2016. Regulation and function of the cGAS-STING pathway of
547 cytosolic DNA sensing. *Nat Immunol* **17**:1142–1149. doi:10.1038/ni.3558
548 Chou TW, Chang NP, Krishnagiri M, Patel AP, Lindman M, Angel JP, Kung PL, Atkins C,
549 Daniels BP. 2021. Fibrillar α-synuclein induces neurotoxic astrocyte activation via RIP
550 kinase signaling and NF-κB. *Cell Death Dis* **12**. doi:10.1038/s41419-021-04049-0
551 Crow YJ, Casanova J-L. 2014. STING-Associated Vasculopathy with Onset in Infancy — A
552 New Interferonopathy. *N Engl J Med* **371**:568–571. doi:10.1056/nejme1407246
553 Decout A, Katz JD, Venkatraman S, Ablasser A. 2021. The cGAS–STING pathway as a
554 therapeutic target in inflammatory diseases. *Nat Rev Immunol* **21**:548–569.
555 doi:10.1038/s41577-021-00524-z
556 Ebrahimi-Fakhari D, Cantuti-Castelvetri I, Fan Z, Rockenstein E, Masliah E, Hyman BT,
557 McLean PJ, Unni VK. 2011. Distinct Roles In Vivo for the Ubiquitin–Proteasome
558 System and the Autophagy–Lysosomal Pathway in the Degradation of α-Synuclein. *J*
559 *Neurosci* **31**:14508. doi:10.1523/JNEUROSCI.1560-11.2011
560 Ejlerskov P, Hultberg JG, Wang JY, Carlsson R, Ambjørn M, Kuss M, Liu Y, Porcu G,
561 Kolkova K, Friis Rundsten C, Ruscher K, Pakkenberg B, Goldmann T, Loreth D, Prinz
562 M, Rubinsztein DC, Issazadeh-Navikas S. 2015. Lack of Neuronal IFN-β-IFNAR
563 Causes Lewy Body- and Parkinson's Disease-like Dementia. *Cell* **163**:324–339.
564 Froula JM, Castellana-Cruz M, Anabtawi NM, Camino JD, Chen SW, Thrasher DR, Freire J,
565 Yazdi AA, Fleming S, Dobson CM, Kumita JR, Cremades N, Volpicelli-Daley LA.
566 2019. Defining α-synuclein species responsible for Parkinson's disease phenotypes in
567 mice. *J Biol Chem* **294**:10392–10406. doi:10.1074/JBC.RA119.007743
568 Fujiwara H, Hasegawa M, Dohmae N, Kawashima A, Masliah E, Goldberg MS, Shen J,
569 Takio K, Iwatsubo T. 2002. α-synuclein is phosphorylated in synucleinopathy lesions.
570 *Nat Cell Biol* **4**:160–164. doi:10.1038/ncb748
571 Gaidt MM, Ebert TS, Chauhan D, Ramshorn K, Pinci F, Zuber S, O'Duill F, Schmid-Burgk
572 JL, Hoss F, Buhmann R, Wittmann G, Latz E, Subklewe M, Hornung V. 2017. The
573 DNA Inflammasome in Human Myeloid Cells Is Initiated by a STING-Cell Death
574 Program Upstream of NLRP3. *Cell* **171**:1110-1124.e18.
575 doi:10.1016/J.CELL.2017.09.039
576 Gal-Ben-Ari S, Barrera I, Ehrlich M, Rosenblum K. 2019. PKR: A kinase to remember.
577 *Front Mol Neurosci* **11**:480. doi:10.3389/FNMOL.2018.00480/BIBTEX
578 Gordon R, Albornoz EA, Christie DC, Langley MR, Kumar V, Mantovani S, Robertson
579 AAB, Butler MS, Rowe DB, O'Neill LA, Kanthasamy AG, Schroder K, Cooper MA,

580 Woodruff TM. 2018. Inflammasome inhibition prevents -synuclein pathology and
581 dopaminergic neurodegeneration in mice. *Sci Transl Med* **10**.
582 doi:10.1126/scitranslmed.aah4066
583 Grozdanov V, Bousset L, Hoffmeister M, Bliederhaeuser C, Meier C, Madiona K, Pieri L,
584 Kiechle M, McLean PJ, Kassubek J, Behrends C, Ludolph AC, Weishaupt JH, Melki R,
585 Danzer KM. 2019. Increased Immune Activation by Pathologic α-Synuclein in
586 Parkinson's Disease. *Ann Neurol* **86**:593–606. doi:10.1002/ana.25557
587 Guzman JN, Sanchez-Padilla J, Wokosin D, Kondapalli J, Ilijic E, Schumacker PT, Surmeier
588 DJ. 2010. Oxidant stress evoked by pacemaking in dopaminergic neurons is attenuated
589 by DJ-1. *Nature* **468**:696–700. doi:10.1038/nature09536
590 Hall S, Janelidze S, Surova Y, Widner H, Zetterberg H, Hansson O. 2018. Cerebrospinal
591 fluid concentrations of inflammatory markers in Parkinson's disease and atypical
592 parkinsonian disorders. *Sci Rep* **8**. doi:10.1038/S41598-018-31517-Z
593 Harms AS, Kordower JH, Sette A, Lindestam Arlehamn CS, Sulzer D, Mach RH. 2021.
594 Inflammation in Experimental Models of α -Synucleinopathies. *Mov Disord* **36**:37–49.
595 doi:10.1002/mds.28264
596 Harris NM, Roy-O'Reilly M, Ritzel RM, Holmes A, Sansing LH, O'Keefe LM, McCullough
597 LD, Chauhan A. 2020. Depletion of CD4 T cells provides therapeutic benefits in aged
598 mice after ischemic stroke. *Exp Neurol* **326**. doi:10.1016/J.EXPNEUROL.2020.113202
599 Heneka MT, McManus RM, Latz E. 2018. Inflammasome signalling in brain function and
600 neurodegenerative disease. *Nat Rev Neurosci* **19**:610–621. doi:10.1038/s41583-018-
601 0055-7
602 Hirsch EC, Standaert DG. 2021. Ten Unsolved Questions About Neuroinflammationnin
603 Parkinson's Disease. *Mov Disord* **36**:16–24. doi:10.1002/mds.28075
604 Hopfner KP, Hornung V. 2020. Molecular mechanisms and cellular functions of cGAS–
605 STING signalling. *Nat Rev Mol Cell Biol* **21**:501–521. doi:10.1038/s41580-020-0244-x
606 Jeffries AM, Marriott I. 2017. Human microglia and astrocytes express cGAS-STING viral
607 sensing components. *Neurosci Lett* **658**:53–56. doi:10.1016/j.neulet.2017.08.039
608 Kovács B, Vajda E, Nagy EE. 2019. Regulatory Effects and Interactions of the Wnt and
609 OPG-RANKL-RANK Signaling at the Bone-Cartilage Interface in Osteoarthritis. *Int J*
610 *Mol Sci* **20**. doi:10.3390/IJMS20184653
611 Kwon HS, Koh SH. 2020. Neuroinflammation in neurodegenerative disorders: the roles of
612 microglia and astrocytes. *Transl Neurodegener* **9**. doi:10.1186/S40035-020-00221-2
613 Li F, Wang N, Zheng Y, Luo Y, Zhang Y. 2021. cGAS- Stimulator of Interferon Genes

614 Signaling in Central Nervous System Disorders. *Aging Dis* **12**:1658–1674.
615 doi:10.14336/AD.2021.0304
616 Li T, Chen ZJ. 2018. The cGAS-cGAMP-STI NG pathway connects DNA damage to
617 inflammation, senescence, and cancer. *J Exp Med* **215**:1287–1299.
618 doi:10.1084/jem.20180139
619 Ling ZD, Potter ED, Lipton JW, Carvey PM. 1998. Differentiation of mesencephalic
620 progenitor cells into dopaminergic neurons by cytokines. *Exp Neurol* **149**:411–423.
621 doi:10.1006/EXNR.1998.6715
622 Liu BC, Sarhan J, Panda A, Muendlein HI, Ilyukha V, Coers J, Yamamoto M, Isberg RR,
623 Poltorak A. 2018. Constitutive Interferon Maintains GBP Expression Required for
624 Release of Bacterial Components Upstream of Pyroptosis and Anti-DNA Responses.
625 *Cell Rep* **24**:155-168.e5. doi:10.1016/J.CELREP.2018.06.012
626 Liu WL, Yang HC, Hsu CS, Wang CC, Wang TS, Kao JH, Chen DS. 2016. Pegylated IFN-α
627 suppresses hepatitis C virus by promoting the DAPK-mTOR pathway. *Proc Natl Acad*
628 *Sci U S A* **113**:14799–14804. doi:10.1073/pnas.1618517114
629 Liu Y, Gordesky-Gold B, Leney-Greene M, Weinbren NL, Tudor M, Cherry S. 2018.
630 Inflammation-Induced, STING-Dependent Autophagy Restricts Zika Virus Infection in
631 the Drosophila Brain. *Cell Host Microbe* **24**:57-68.e3. doi:10.1016/j.chom.2018.05.022
632 Liu Y, Jesus AA, Marrero B, Yang D, Ramsey SE, Montealegre Sanchez GA, Tenbrock K,
633 Wittkowski H, Jones OY, Kuehn HS, Lee C-CR, DiMattia MA, Cowen EW, Gonzalez
634 B, Palmer I, DiGiovanna JJ, Biancotto A, Kim H, Tsai WL, Trier AM, Huang Y, Stone
635 DL, Hill S, Kim HJ, St. Hilaire C, Gurprasad S, Plass N, Chapelle D, Horkayne-Szakaly
636 I, Foell D, Barysenka A, Candotti F, Holland SM, Hughes JD, Mehmet H, Issekutz AC,
637 Raffeld M, McElwee J, Fontana JR, Minniti CP, Moir S, Kastner DL, Gadina M, Steven
638 AC, Wingfield PT, Brooks SR, Rosenzweig SD, Fleisher TA, Deng Z, Boehm M, Paller
639 AS, Goldbach-Mansky R. 2014. Activated STING in a vascular and pulmonary
640 syndrome. *N Engl J Med* **371**:507–518. doi:10.1056/NEJMOA1312625
641 Luksch H, Stinson WA, Platt DJ, Qian W, Kalugotla G, Miner CA, Bennion BG, Gerbaulet
642 A, Rösen-Wolff A, Miner JJ. 2019. STING-associated lung disease in mice relies on T
643 cells but not type I interferon. *J Allergy Clin Immunol* **144**:254-266.e8.
644 doi:10.1016/j.jaci.2019.01.044
645 Magalhaes J, Tresse E, Ejlerskov P, Hu E, Liu Y, Marin A, Montalant A, Satriano L,
646 Rundsten CF, Carlsen EMM, Rydbirk R, Sharifi-Zarchi A, Andersen JB, Aznar S,
647 Brudek T, Khodosevich K, Prinz M, Perrier JFM, Sharma M, Gasser T, Issazadeh-

648 Navikas S. 2021. PIAS2-mediated blockade of IFN-β signaling: a basis for sporadic
649 Parkinson disease dementia. *Mol Psychiatry 2021* 1–17. doi:10.1038/s41380-021-
650 01207-w
651 Mejias NH, Martinez CC, Stephens ME, De Rivero Vaccari JP. 2018. Contribution of the
652 inflammasome to inflammaging. *J Inflamm (United Kingdom)* **15**:1–10.
653 doi:10.1186/S12950-018-0198-3/FIGURES/6
654 Mollenhauer B, Zimmermann J, Sixel-Döring F, Focke NK, Wicke T, Ebentheuer J,
655 Schaumburg M, Lang E, Friede T, Trenkwalder C. 2019. Baseline predictors for
656 progression 4 years after Parkinson's disease diagnosis in the De Novo Parkinson
657 Cohort (DeNoPa). *Mov Disord* **34**:67–77. doi:10.1002/mds.27492
658 Moretti J, Roy S, Bozec D, Martinez J, Chapman JR, Ueberheide B, Lamming DW, Chen ZJ,
659 Horng T, Yeretssian G, Green DR, Blander JM. 2017. STING Senses Microbial
660 Viability to Orchestrate Stress-Mediated Autophagy of the Endoplasmic Reticulum. *Cell*
661 **171**:809-823.e13. doi:10.1016/j.cell.2017.09.034
662 Motwani M, Pesiridis S, Fitzgerald KA. 2019. DNA sensing by the cGAS–STING pathway
663 in health and disease. *Nat Rev Genet* **20**:657–674. doi:10.1038/s41576-019-0151-1
664 Nazmi A, Field RH, Griffin EW, Haugh O, Hennessy E, Cox D, Reis R, Tortorelli L, Murray
665 CL, Lopez-Rodriguez AB, Jin L, Lavelle EC, Dunne A, Cunningham C. 2019. Chronic
666 neurodegeneration induces type I interferon synthesis via STING, shaping microglial
667 phenotype and accelerating disease progression. *Glia* **67**:1254–1276.
668 doi:10.1002/glia.23592
669 Neumann M, Kahle PJ, Giasson BI, Ozmen L, Borroni E, Spooren W, Müller V, Odoy S,
670 Fujiwara H, Hasegawa M, Iwatsubo T, Trojanowski JQ, Kretzschmar HA, Haass C.
671 2002. Misfolded proteinase K-resistant hyperphosphorylated alpha-synuclein in aged
672 transgenic mice with locomotor deterioration and in human alpha-synucleinopathies. *J*
673 *Clin Invest* **110**:1429–1439. doi:10.1172/JCI15777
674 Noguchi S, Yamada N, Kumazaki M, Yasui Y, Iwasaki J, Naito S, Akao Y. 2013. socs7, a
675 target gene of microRNA-145, regulates interferon-β induction through STAT3 nuclear
676 translocation in bladder cancer cells. *Cell Death Dis* **4**:e482.
677 doi:10.1038/CDDIS.2013.11
678 Obeso JA, Stamelou M, Goetz CG, Poewe W, Lang AE, Weintraub D, Burn D, Halliday GM,
679 Bezard E, Przedborski S, Lehericy S, Brooks DJ, Rothwell JC, Hallett M, DeLong MR,
680 Marras C, Tanner CM, Ross GW, Langston JW, Klein C, Bonifati V, Jankovic J,
681 Lozano AM, Deuschl G, Bergman H, Tolosa E, Rodriguez-Violante M, Fahn S,

682 Postuma RB, Berg D, Marek K, Standaert DG, Surmeier DJ, Olanow CW, Kordower
683 JH, Calabresi P, Schapira AHV, Stoessl AJ. 2017. Past, present, and future of
684 Parkinson's disease: A special essay on the 200th Anniversary of the Shaking Palsy.
685 *Mov Disord*. doi:10.1002/mds.27115
686 Olsen LK, Cairns AG, Ådén J, Moriarty N, Cabre S, Alamilla VR, Almqvist F, Dowd E,
687 McKernan DP. 2019. Viral mimetic priming enhances α-synuclein-induced
688 degeneration: Implications for Parkinson's disease. *Brain Behav Immun* **80**:525–535.
689 doi:10.1016/j.bbi.2019.04.036
690 Paul BD, Snyder SH, Bohr VA. 2021. Signaling by cGAS–STING in Neurodegeneration,
691 Neuroinflammation, and Aging. *Trends Neurosci* **44**:83–96.
692 doi:10.1016/j.tins.2020.10.008
693 Paxinos G, Franklin KBJ. 2001. Paxinos and Franklin's the Mouse Brain in Stereotaxic
694 Coordinates, Academic Press.
695 Reimer L, Vesterager LB, Betzer C, Zheng J, Nielsen LD, Kofoed RH, Lassen LB, Bølcho U,
696 Paludan SR, Fog K, Jensen PH. 2018. Inflammation kinase PKR phosphorylates α-
697 synuclein and causes α-synuclein-dependent cell death. *Neurobiol Dis* **115**:17–28.
698 doi:10.1016/J.NBD.2018.03.001
699 Rodriguez-Pallares J, Guerra MJ, Labandeira-Garcia JL. 2005. Angiotensin II and
700 interleukin-1 interact to increase generation of dopaminergic neurons from neurospheres
701 of mesencephalic precursors. *Brain Res Dev Brain Res* **158**:120–122.
702 doi:10.1016/J.DEVBRAINRES.2005.06.009
703 Samuel F, Flavin WP, Iqbal S, Pacelli C, Renganathan SDS, Trudeau LE, Campbell EM,
704 Fraser PE, Tandon A. 2016. Effects of Serine 129 Phosphorylation on α-Synuclein
705 Aggregation, Membrane Association, and Internalization. *J Biol Chem* **291**:4374.
706 doi:10.1074/JBC.M115.705095
707 Schroder K, Tschopp J. 2010. The Inflammasomes. *Cell* **140**:821–832.
708 doi:10.1016/j.cell.2010.01.040
709 Sen T, Saha P, Gupta R, Foley LM, Jiang T, Abakumova OS, Hitchens TK, Sen N. 2020.
710 Aberrant ER Stress-Induced Neuronal-IFNβ Elicits White Matter Injury Due to
711 Microglial Activation and T-Cell Infiltration after TBI. *J Neurosci Off J Soc Neurosci*
712 **40**:424–446. doi:10.1523/JNEUROSCI.0718-19.2019
713 Siedel H, Roers A, Rösen-Wolff A, Luksch H. 2020. Type I interferon-independent T cell
714 impairment in a Tmem173 N153S/WT mouse model of STING associated vasculopathy
715 with onset in infancy (SAVI). *Clin Immunol* **216**:108466.

716 doi:10.1016/j.clim.2020.108466
717 Sliter DA, Martinez J, Hao L, Chen X, Sun N, Fischer TD, Burman JL, Li Y, Zhang Z,
718 Narendra DP, Cai H, Borsche M, Klein C, Youle RJ. 2018. Parkin and PINK1 mitigate
719 STING-induced inflammation. *Nature*. doi:10.1038/s41586-018-0448-9
720 Spandidos A, Wang X, Wang H, Seed B. 2009. PrimerBank: A resource of human and mouse
721 PCR primer pairs for gene expression detection and quantification. *Nucleic Acids Res*
722 **38**:D792–D799.
723 Szegő ÉM, Boß F, Komnig D, Gärtner C, Höfs L, Shaykhalishahi H, Woerdehoff M, Saridaki
724 T, Schulz JB, Hoyer W, Falkenburger BH. 2021. A β-wrapin targeting the N-terminus of
725 α-synuclein monomers reduces fibril-induced aggregation in neurons. *Front Neurosci*
726 **15**:751.
727 Szegő ÉM, Gerhardt E, Kermer P, Schulz JB. 2012. A30P α-synuclein impairs dopaminergic
728 fiber regeneration and interacts with L-DOPA replacement in MPTP-treated mice.
729 *Neurobiol Dis* **45**:591–600.
730 Szegő ÉM, Gerhardt E, Outeiro TF. 2017. Sirtuin 2 enhances dopaminergic differentiation
731 via the AKT/GSK-3β/β-catenin pathway. *Neurobiol Aging* **56**:7–16.
732 Szegö EM, Van den Haute C, Höfs L, Baekelandt V, Van der Perren A, Falkenburger BH.
733 2022. Rab7 reduces α-synuclein toxicity in rats and primary neurons. *Exp Neurol*
734 **347**:113900. doi:10.1016/J.EXPNEUROL.2021.113900
735 von Herrmann KM, Salas LA, Martinez EM, Young AL, Howard JM, Feldman MS,
736 Christensen BC, Wilkins OM, Lee SL, Hickey WF, Havrda MC. 2018. NLRP3
737 expression in mesencephalic neurons and characterization of a rare NLRP3
738 polymorphism associated with decreased risk of Parkinson's disease. *npj Park Dis* **4**:24.
739 doi:10.1038/s41531-018-0061-5
740 Wang W, Hu D, Wu C, Feng Y, Li A, Liu W, Wang Y, Chen K, Tian M, Xiao F, Zhang Q,
741 Shereen MA, Chen W, Pan P, Wan P, Wu K, Wu J. 2020. STING promotes NLRP3
742 localization in ER and facilitates NLRP3 deubiquitination to activate the inflammasome
743 upon HSV-1 infection. *PLoS Pathog* **16**. doi:10.1371/JOURNAL.PPAT.1008335
744 Warner JD, Irizarry-Caro RA, Bennion BG, Ai TL, Smith AM, Miner CA, Sakai T,
745 Gonugunta VK, Wu J, Platt DJ, Yan N, Miner JJ. 2017. STING-associated vasculopathy
746 develops independently of IRF3 in mice. *J Exp Med* **214**:3279–3292.
747 doi:10.1084/JEM.20171351
748 West AP, Khoury-Hanold W, Staron M, Tal MC, Pineda CM, Lang SM, Bestwick M,
749 Duguay BA, Raimundo N, MacDuff DA, Kaech SM, Smiley JR, Means RE, Iwasaki A,

750 Shadel GS. 2015. Mitochondrial DNA stress primes the antiviral innate immune
751 response. *Nature* **520**:553–557. doi:10.1038/nature14156
752 Wolf SA, Boddeke HWGM, Kettenmann H. 2017. Microglia in Physiology and Disease.
753 *Annu Rev Physiol* **79**:619–643. doi:10.1146/ANNUREV-PHYSIOL-022516-034406
754

755 ## Figure Legends

756 **Figure 1. Constitutive STING activation induces neuroinflammation and**
757 **neurodegeneration in adult mice.**

758 (A) Representative images of striatal sections from STING WT and STING ki mice stained for
759 the microglia marker Iba1. Scale bar: 50 µm. (B) Representative images of striatal sections
760 stained for the astroglia marker GFAP. Scale bar: 50 µm. (C) Representative images of
761 midbrain sections containing the *substantia nigra* (SN) from STING WT and STING ki mice
762 (stitched from two microscopy fields) stained for tyrosine hydroxylase (TH). Scale bar: 100
763 µm. (D) Representative images of striatal sections stained for TH from STING WT and STING
764 ki mice. Scale bar: 10 µm. (E) Area fraction positive for Iba1, normalized to the mean of STING
765 WT mice. Markers represent individual animals (black: STING WT animals, red: STING ki
766 animals). Lines represent mean ± SD. Comparison by t-test (***: p=0,0007). (F) Area fraction
767 positive for GFAP, normalized to the mean of STING WT mice (**: p=0,0011; t-test). (G)
768 Number of TH-positive neurons (*: p=0,0257; t-test). (H) Area fraction positive for TH (**:
769 p=0,0081; t-test). (I) Concentration of dopamine (*: p=0,0448; t-test) in striatal lysates from
770 STING WT and STING ki animals, normalized to the mean concentration in STING WT.
771 Graphs showing quantification of the dopamine metabolites are in figure supplement 1B.

772

773 **Figure 2. Neuroinflammation without neurodegeneration in juvenile mice with**
774 **constitutive STING activation.**

775 (A) Representative images of striatal sections stained for the microglia marker Iba1 from 5
776 week-old STING WT and STING ki mice. Scale bar: 50 µm (B) Representative images of
777 striatal sections stained for the astroglia marker GFAP from 5 week-old STING WT and
778 STING ki mice. Scale bar: 50 µm (C) Representative images of midbrain sections containing
779 the *substantia nigra* (SN, stitched from two microscopy fields) stained for tyrosine hydroxylase
780 (TH) from 5 week-old STING WT and STING ki mice. Scale bar: 100 µm (D) Representative
781 images of striatal sections stained for TH from 5 week-old STING WT and STING ki mice.
782 Scale bar: 10 µm. (E) Area fraction positive for Iba1, normalized to the mean of STING WT
783 (***: p=0,0009; t-test). (F) Area fraction positive for GFAP, normalized to the mean of STING
784 WT brains (***: p=0,0007; t-test). (G) Number of TH-positive neurons (mean ± SD; t-test).
785 (H) Area fraction positive for TH (mean ± SD, t-test). (I) Dopamine concentration in striatal
786 lysates from 5 week-old STING WT and STING ki mice, measured by HPLC and normalized

787 to the mean of STING WT (mean ± SD, t-test). Dopamine metabolites are in figure supplement
788 1D.
789
790 **Figure 3. Constitutive STING activation induces alpha-synuclein pathology and synapse**
791 **loss in adult mice.**
792 (A) Representative Western blot images showing phosphorylated alpha-synuclein (S129;
793 paSyn, upper panel), total alpha-synuclein (aSyn, middle panel) and the loading control βIII-
794 tubulin (lower panel). (B) Representative images of striatal sections from 20 week-old STING
795 WT and STING ki mice stained with Thioflavin S. Scale bar: 10 µm (C) Ratio of total alpha-
796 synuclein and loading control, expressed relative to the mean of STING WT (p=0,0491; mean
797 ± SD; t-test). (D) Immunoreactivity to paSyn and aSyn, expressed relative to the mean of
798 STING WT (p=0,0059; mean ± SD; t-test). (E) Number of cells with inclusions positive for
799 Thioflavin S (ThioS) per mm^2 (*: p=0,0141; t-test). (F-G) Representative images of striatal
800 sections from 20 week-old STING WT and STING ki mice stained for the presynaptic marker
801 synapsin (F) or for the post-synaptic marker homer (G). Scale bar: 10 µm. (H-I) Area fraction
802 positive for synapsin (H, p=0,0053) or homer (I, p=0,0408) (mean ± SD; t-test).
803
804 **Figure 4. Activation of IFN and NF-κB/inflammasome dependent signaling in juvenile**
805 **and adult STING ki mice.**
806 (A-D) Expression of ISGs in the frontal cortex of STING WT and STING ki mice. (A) *Ifi44*
807 (***: p=0,0002277; *: p= 0,044987), (B) *Mx-1* (***: p=0,0000003; *: p= 0,016835; for
808 comparison between age groups ***: p= 0,000602), (C) *Ip-10* (***: p= 0,000001; **: p=
809 0,0017215; for comparison between age groups **: p= 0,001483), (D) *Sting1* (*: p=
810 0,0184042). (E-G) Expression of NF-κB/inflammasome related genes in the frontal cortex of
811 STING WT and STING ki mice. (E) *Tnfα* (***: p= 0,0001448, for comparison between age
812 groups *: p= 0,03952). (F) *Il-1b* (***: p= 0,00005, *: p= 0,0389, for comparison between age
813 groups **: p= 0,00241). (G) *Casp1* (***: p= 0,0000369, for comparison between age groups
814 ***: p= 0,000064). Markers represent individual animals, bars represent mean ± SD. Analysis
815 was two-way ANOVA with Tukey HSD post-hoc test.
816
817 **Figure 5. Nuclear translocation of pSTAT3 and NF-κB in the striatum of 5 and 20 week-**
818 **old STING WT and STING ki mice.**
819 (A) Representative images of striatal sections from 5 week-old (upper images) and 20 week-
820 old (lower images) STING WT and STING ki mice stained for Iba1 (green), GFAP (white) and

821 phosphorylated-STAT3 (pSTAT3; red). Images show color coded merged channels (center)
822 and in addition pSTAT3 staining in grayscale (left and right). Scale bar: 10 µm. (B)
823 Representative images of striatal sections from 4 week-old (upper images) and 20 week-old
824 (lower images) STING WT and STING ki mice stained for Iba1 (green), GFAP (white) and
825 NF-κB (red) . NF-kB staining is shown in gray in separate images. Scale bar: 10 µm. (C)
826 Number of pSTAT3-positive nuclei/mm^3 (***: p=0,00004; **: p=0,0025 for the interaction;
827 two-way ANOVA, Bonferroni post-hoc test). (D) Number of NF-kB-positive nuclei/mm^3 (**:
828 p=0,009; ***: p=0,0007; mean ± SD; two-way ANOVA, Bonferroni post-hoc test).
829
830 **Figure 6. Neuroinflammation in adult double transgenic mice with STING ki and knock-**
831 **out for Ifnar1 or Caspase-1.**
832 (A-E) Expression of IFN related genes and NF-κB/inflammasome related genes in the frontal
833 cortex of adult STING WT and STING ki mice (ANOVA with Tukey HSD post-hoc test). (A)
834 *Ifi44* (*: p= 0,01414; **: p= 0,0037655; for interaction between Ctrl. and and *Ifnar1*$^{-/-}$, **: p=
835 0,005101). (B) *Mx-1* (*: p= 0,02823; **: p= 0,00573). (C) *Il-1b* (Ctrl. background *: p=
836 0,04534; **: p= 0, 005405; *Casp1*$^{-/-}$ *background* *: p= 0,0107096; for interaction between Ctrl.
837 and *Casp1*$^{-/-}$, *: p= 0,01298). (D) *Ip-10* (Ctrl. background **: p= 0,0030844; *Ifnar1*$^{-/-}$
838 background: p= 0,025893; *Casp1*$^{-/-}$ *background* **: p= 0,0041598). (E) *Tnfα* (all differences
839 n.s.). *Sting1* expression is shown on figure supplement 2A. (F) Representative images of striatal
840 sections stained for the microglia marker Iba1. Sections were obtained from adult STING WT
841 (upper images) or STING ki (lower images) mice on a background of interferon a receptor
842 knockout (*Ifnar1*$^{-/-}$), caspase 1 knockout (*Casp1*$^{-/-}$) or *Ifnar1*$^{+/+}$, *Casp1*$^{+/+}$ (Ctrl.). Scale bar: 50
843 µm. (G) Representative images of striatal sections stained for the astroglia marker GFAP from
844 STING WT (upper images) or STING ki (lower images) mice on a background of interferon a
845 receptor knockout (*Ifnar1*$^{-/-}$), caspase 1 knockout (*Casp1*$^{-/-}$) or *Ifnar1*$^{+/+}$, *Casp1*$^{+/+}$ (Ctrl.). Scale
846 bar: 50 µm. (H) Area fraction positive for Iba1, normalized to the mean of STING WT brains
847 (differences in $^{+/+}$ mice ***: p= 0,0000001; for *Ifnar1*$^{-/-}$ ***: p=0,000003; for *Casp1*$^{-/-}$ ***: p=
848 0,0029374; two-way ANOVA with Bonferroni post-hoc test). (I) Area fraction positive for
849 GFAP, normalized to STING WT on Ctrl. Background (***: p= 0,0000 for STING WT vs
850 STING ki on Ctrl.; ***: p= 0,0000 on *Ifnar1*$^{-/-}$; background, ***: p=xyz on Casp1-/-
851 background; two-way ANOVA with Bonferroni post-hoc test).
852
853 **Figure 7. Degeneration of dopaminergic neurons in double transgenic mice with STING**
854 **N153S/WT ki and knock-out for Ifnar1 or Caspase-1.**

855 (A) Representative images of striatal sections stained for tyrosine hydroxylase (TH) from
856 STING WT (upper images) or STING ki (lower images) mice on a background of interferon a
857 receptor knockout (*Ifnar1*$^{-/-}$), caspase-1 knockout (*Casp1*$^{-/-}$) or *Ifnar1*$^{+/+}$, *Casp1*$^{+/+}$ (Ctrl.). Scale
858 bar: 10 µm. (B) Area fraction positive for TH, normalized to STING WT on Ctrl. background
859 (***: p=0,0000 for Ctrl. background; *: p= 0,043 for *Ifnar1*$^{-/-}$; **: p=0,0126845 for *Casp1*$^{-/-}$;
860 for interaction between Ctrl. background and *Ifnar1*$^{-/-}$: p= 0,00157; between Ctrl. and *Casp1*$^{-/-}$
861 : p= 0,007326; two-way ANOVA with Bonferroni post-hoc test). (C) Concentration of
862 dopamine in striatal lysates of STING WT and STING ki mice, normalized to STING WT on
863 Ctrl. background. (***: p= 0,0005; t-test). Dopamine metabolism is shown on figure
864 supplement 2B.

865 **Supplemental Information**

866 **Figure supplement 1, related to Figures 1 and 2. Number of TH-positive neurons in the**
867 ***substantia nigra* and dopamine metabolism in the striatum of STING WT and STING ki**
868 **mice**

869 (A) Number of TH-positive neurons in the substantia nigra of adult mice (p=0,0257; t-test). (B)
870 Dopamine metabolism (concentration of dopamine metabolites DOPAC + HVA) / dopamine
871 in adult mice (p=0,0179; t-test). (C) Number of TH-positive neurons in the substantia nigra of
872 juvenile mice (p=0,5188; t-test). (D) Dopamine metabolism in juvenile mice (p=0,9545; t-test).

873

874

875 **Figure supplement 2, related to Figures 6 and 7. *Sting1* expression and dopamine**
876 **metabolism in KO animals.**

877 (A) Expression of *Sting1* in the frontal cortex of STING WT and STING ki mice on a
878 background of interferon a receptor knockout (*Ifnar1*$^{-/-}$), caspase 1 knockout (*Casp1*$^{-/-}$) or
879 *Ifnar1*$^{+/+}$, *Casp1*$^{+/+}$ (Ctrl.). (all differences n.s., 2-way ANOVA). (B) Dopamine metabolism
880 in STING WT and STING ki mice. (**: p= 0,0073; 2-way ANOVA).

881 **Supplemental Table S1.– List of materials and antibody dilutions**

Antibody	Dilution	Source	ID
Anti-Iba1, rabbit	1:1000	Fujifilm Wako Chemicals	Cat# 019-19741
Anti-GFAP, chicken	1:2000	Abcam	Cat# ab4674
Anti-NFκB p65 (D14E12), rabbit	1:500	Cell Signaling Technology	Cat# 8242
Anti-Tubulin βIII, rabbit	1:5000	Covance	Cat# PRB-435P
Anti-phospho-a-synuclein, rabbit	1:1000	Abcam	Cat# ab51253
Anti-a-synuclein, mouse	1:2000	BD Biosciences	Cat# 610787
Anti-TH, sheep	1:2000	Pel Freez	Cat# P40101
Anti-homer, rabbit	1.1000	Synaptic Systems	Cat# 160002
Anti-Synapsin, chicken	1:1000	Synaptic System	Cat# 106006
HRP conjugated donkey anti-mouse IgG	1:5000	Jackson ImmunoResearch	Cat# 715-035-150
HRP conjugated donkey anti-rabbit IgG	1:5000	Jackson ImmunoResearch	Cat# 711-035-152
Alexa 555 conjugated donkey anti-rabbit	1:2000	Invitrogen	Cat# A31572
Alexa 647 conjugated donkey anti-chicken	1:2000	Jackson ImmunoResearch	Cat# 703-605-155
Alexa 488 conjugated donkey anti-sheep	1:2000	Invitrogen	Cat# A11015
Alexa 488 conjugated donkey anti-rabbit	1:2000	Invitrogen	Cat# A21206
Reagent			
PhosSTOP phosphatase inhibitor		Sigma-Aldrich	Cat# 4906845001
Bromphenol blue		Honeywell Fluka	Cat# 32712
Mini-PROTEAN TGX Precast Gels 4-20%		BioRad	Cat# 4561094
Precision Plus Protein WesternC Protein Standards		BioRad	Cat# 1610376
WesternBright Chemilumineszenz Substrat Sirius		Biozym Scientific GmbH	Cat# 541019
M-MLV Reverse Transriptase		Promega	Cat# M1701
RNasin Ribonuclease Inhibitor		Promega	Cat# N2511
GoTaq® qPCR Master Mix		Promega	Cat# A6002
Deoxynucleotide Triphosphates (dNTPs)		Promega	Cat# U1205
M-MLV 5x Reaction Buffer		Promega	Cat# M1701
Pierce Micro BCA Protein-Assay-Kit		Thermo Fisher Scientific Inc.	Cat# 23235
SV Total RNA Isolation System		Promega	Cat# Z3101
Fluoromount-G		Southern Biotech	Cat# 0100-01
Equipment			
Infinite 200M Multimode-Plate-Reader		Tecan Group	
QuantStudio 5 Real-Time PCR System		Thermo Fisher Scientific Inc.	
CM3050S Kryostat		Leica Mikrosysteme Vertrieb GmbH	
Zeiss Axio Observer Z1		Carl Zeiss	
Zeiss Spinning Disc		Carl Zeiss	
Software			
GraphPad Prism 5. 01 and 9.0.0		GraphPad Software	
ImageJ Fiji		Wayne Rasband (NIH)	
QuantStudio5 qPCR Data Analysis Software		Thermo Fisher Scientific Inc.	

882

Supplemental Table S2. – List of qRT PCR Primers

Gene	Primer forward (5' - 3')	Primer revers (5' - 3')
Ifi44	*AACTGACTGCTCGCAATAATGT*	*GTAACACAGCAATGCCTCTTGT*
Mx-1	AACCCTGCTACCTTTCAA	AAGCATCGTTTTCTCTATTTC
Sting1	CTGCTGACATATACCTCAGTTG	GAGCATGTTGTTATGTAGCTG
Ip-10	CCAAGTGCTGCCGTCATTTTC	GGCTCGCAGGGATGATTTCAA
Tnfα	CCTGTAGCCCACGTCGTAG	GGGAGTAGACAAGGTACAACCC
Casp1	GCTGCCTGCCCAGAGCACAAG	CTCTTCAGAGTCTCTTACTG
Il-1β	GAAATGCCACCTTTTGACAGTG	TGGATGCTCTCATCAGGACAG
Hprt1	TCAGTCAACGGGGGACATAAA	GGGGCTGTACTGCTTAACCAG
Rpl13a	AGCCTACCAGAAAGTTTGCTTAC	GCTTCTTCTTCCGATAGTGCATC
Eef2	CCGACTCCCTTGTGTGCAA	AGTTCAGGTCGTTCTCAGAGAG

Supplemental Table S4. – Sample numbers in each analysis

Assay	Group -- number of animals used/excluded						Reason*
Western blot	**STING WT adult**	**STING ki adult**					
	5/0	5/0					
qPCR	**STING WT adult**	**STING ki adult**	**STING WT juvenile**	**STING ki juvenile**			
Ifi44	5/0	5/0	5/0	5/0			
Ip-10	4/1	4/1	5/0	5/0			Outlier
Mx-1	4/1	4/1	5/0	5/0			Outlier
Tnfa1	5/0	5/0	5/0	5/0			
Casp1	5/0	4/1	5/0	5/0			Outlier
Il-1b	4/1	5/0	4/1	5/0			Outlier
Sting1	5/0	5/0	5/0	4/1			Outlier
	STING WT	**STING ki**	**STING WT *Ifnar1*$^{-/-}$**	**STING ki *Ifnar1*$^{-/-}$**	**STING WT *Casp1*$^{-/-}$**	**STING ki *Casp1*$^{-/-}$**	
Ifi44	5/0	5/0	5/0	5/0	4/1	5/0	Outlier
Ip-10	4/1	4/1	4/1	4/1	4/1	4/1	Outlier
Mx-1	4/1	4/1	4/1	5/0	5/0	5/0	Outlier
Tnfa1	5/0	5/0	5/0	4/1	5/0	5/0	Outlier
Il6	4/1	5/0	5/0	4/1	4/1	4/1	Outlier
Casp1	5/0	5/0	5/0	5/0	5/0	5/0	Outlier
Il-1b	5/0	5/0	4/1	5/0	4/1	5/0	Outlier
Histology	**STING WT adult**	**STING ki adult**	**STING WT juvenile**	**STING ki juvenile**			
	5/0	5/0	5/0	6/0			
	STING WT	**STING ki**	**STING WT, *Ifnar1*$^{-/-}$**	**STING ki, *Ifnar1*$^{-/-}$**	**STING WT, *Casp1*$^{-/-}$**	**STING ki, *Casp1*$^{-/-}$**	
	5/0	5/0	5/0	6/0	5/0	5/0	
HPLC	**STING WT adult**	**STING ki adult**	**STING WT juvenile**	**STING ki juvenile**			
	5/0	5/0	5/0	5/0			
	STING WT	**STING ki**	**STING WT, *Ifnar1*$^{-/-}$**	**STING ki, *Ifnar1*$^{-/-}$**	**STING WT, *Casp1*$^{-/-}$**	**STING ki, *Casp1*$^{-/-}$**	
	8/0	7/0	3/0	3/0	9/0	6/0	

*Grubbs`test was used to detect outliers (Prism).

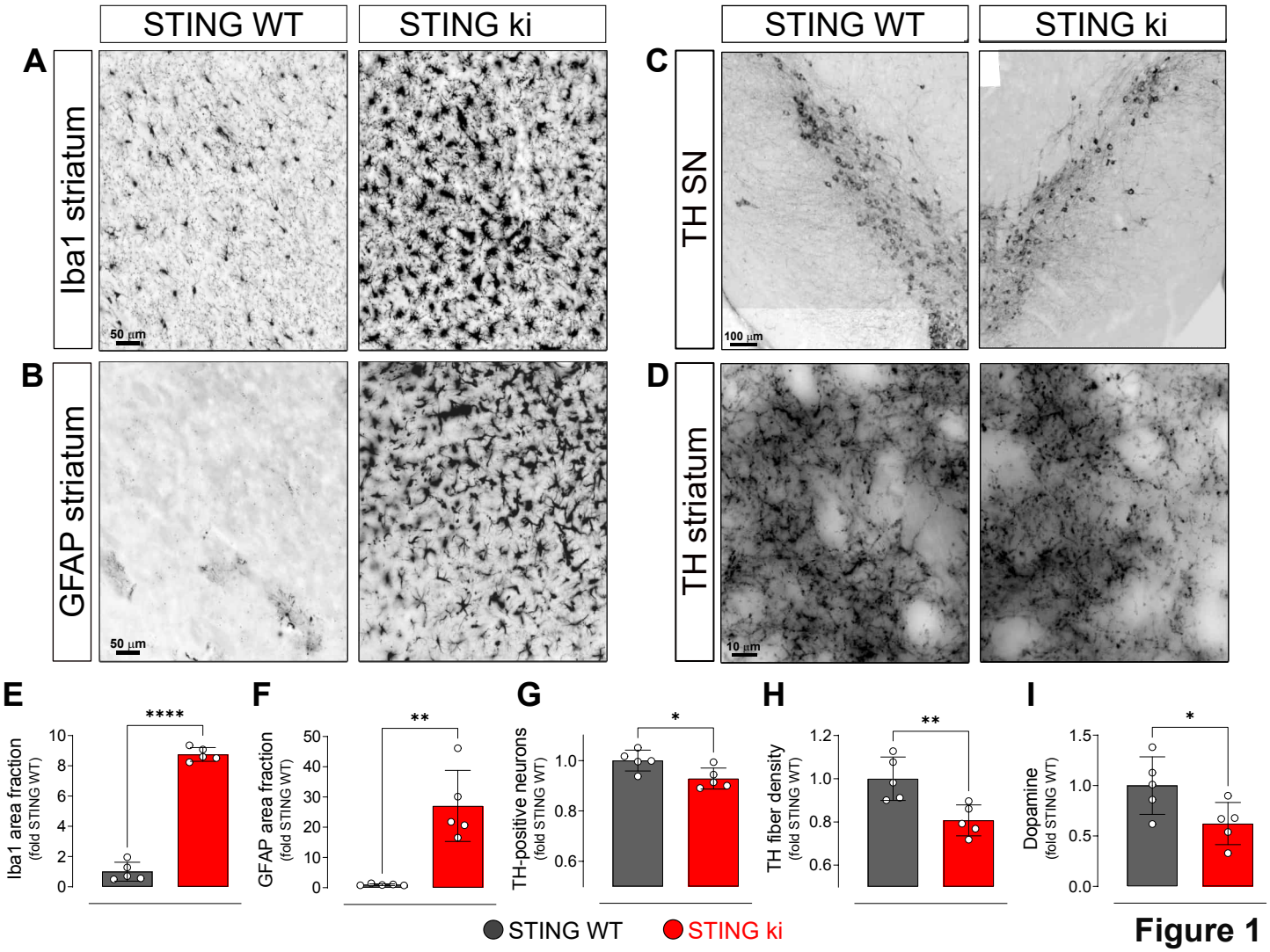
STING WT
STING ki
A
Iba1 striatum
50 µm
B
GFAP striatum
50 µm
STING WT
STING ki
C
TH SN
100 µm
D
TH striatum
10 µm
E
Iba1 area fraction
(fold STING WT)
****
F
GFAP area fraction
(fold STING WT)
**
G
TH-positive neurons
(fold STING WT)
*
H
TH fiber density
(fold STING WT)
**
I
Dopamine
(fold STING WT)
*
STING WT
STING ki

Figure 1

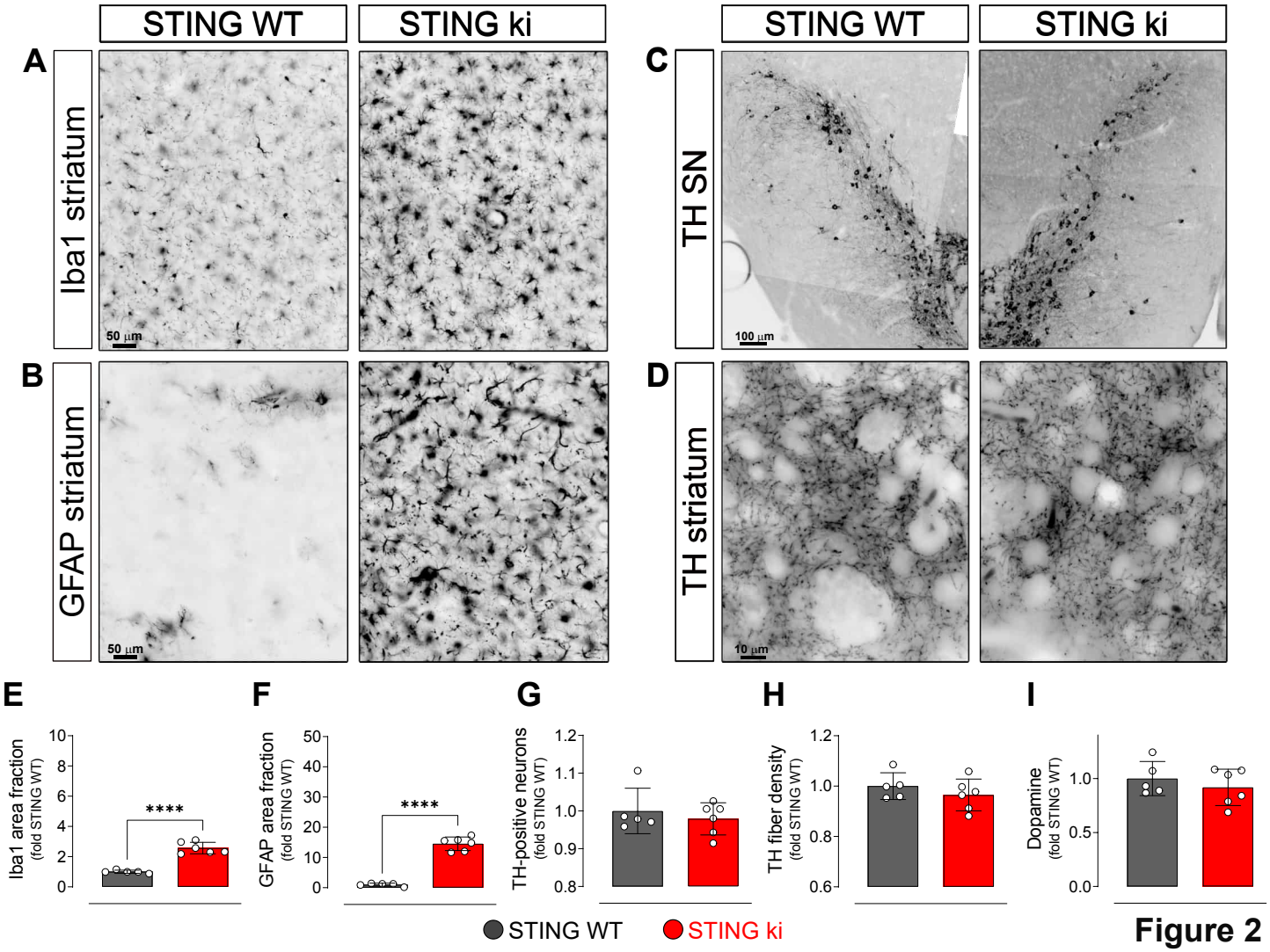
STING WT
STING ki
A
Iba1 striatum
50 µm
B
GFAP striatum
50 µm
STING WT
STING ki
C
TH SN
100 µm
D
TH striatum
10 µm
E
Iba1 area fraction
(fold STING WT)
****
F
GFAP area fraction
(fold STING WT)
****
G
TH-positive neurons
(fold STING WT)
H
TH fiber density
(fold STING WT)
I
Dopamine
(fold STING WT)
STING WT
STING ki

Figure 2

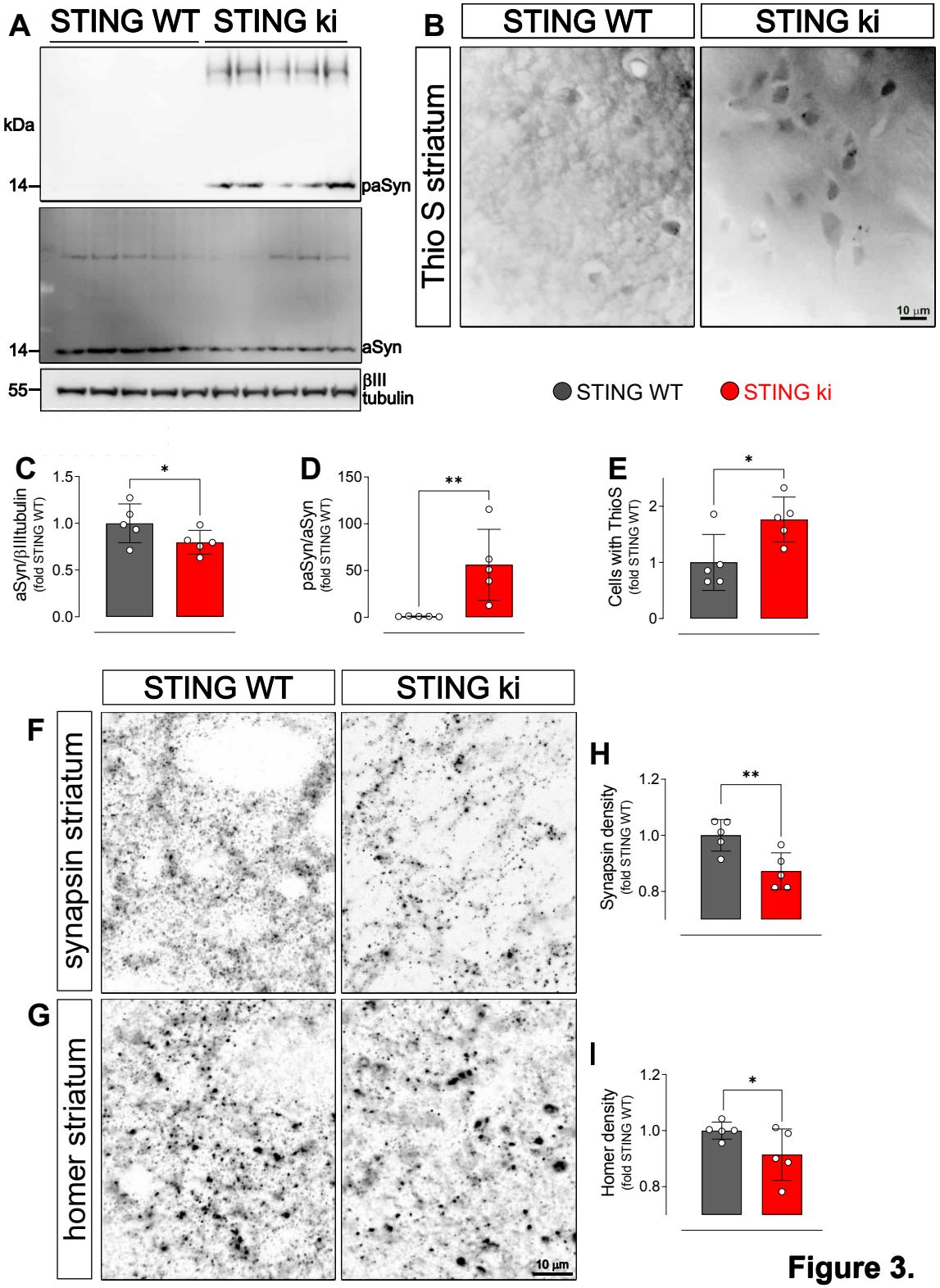
A
STING WT
STING ki
kDa
14
paSyn
14
aSyn
55
βIII tubulin
B
STING WT
STING ki
Thio S striatum
10 µm
STING WT
STING ki
C
aSyn/βIIItubulin (fold STING WT)
1.5
1.0
0.5
0.0
*
D
paSyn/aSyn (fold STING WT)
150
100
50
0
**
E
Cells with ThioS (fold STING WT)
2
1
0
*
STING WT
STING ki
F
synapsin striatum
G
homer striatum
10 µm
H
Synapsin density (fold STING WT)
1.2
1.0
0.8
**
I
Homer density (fold STING WT)
1.2
1.0
0.8
*

Figure 3.

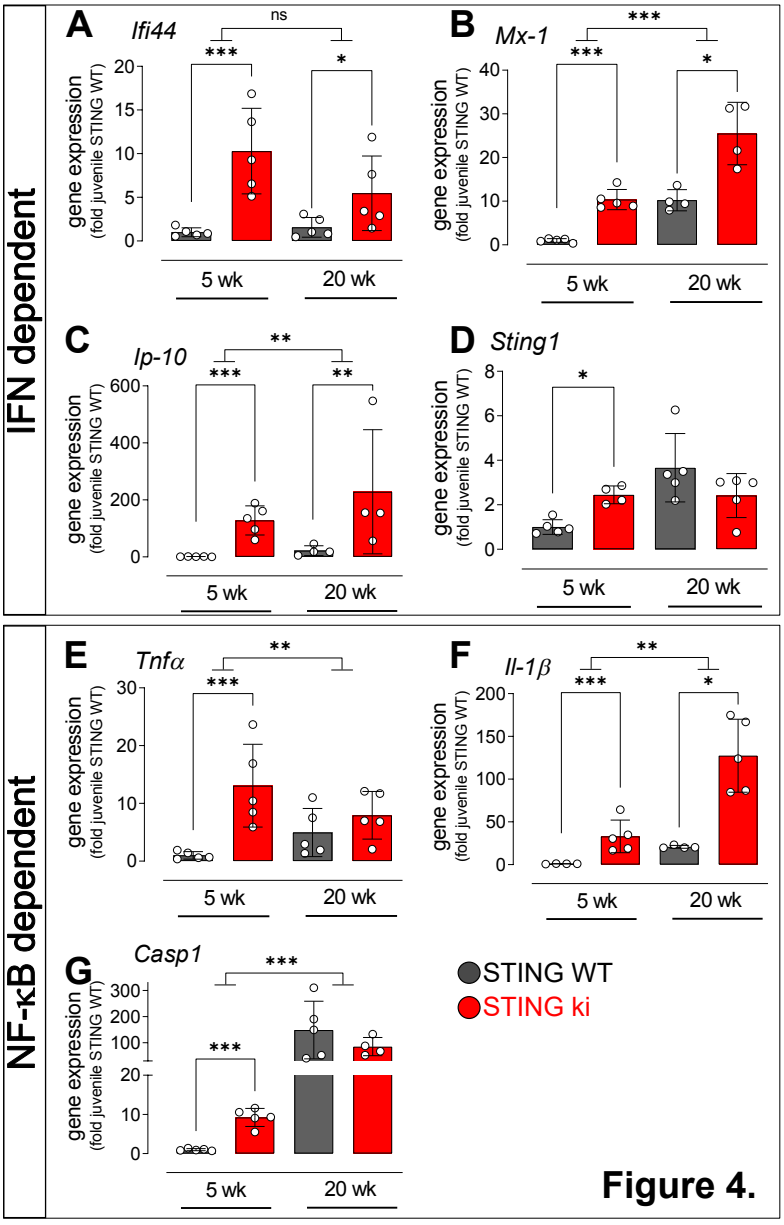
IFN dependent
A
Ifi44
ns
***
*
gene expression
(fold juvenile STING WT)
20
15
10
5
0
5 wk
20 wk
B
Mx-1
***
***
*
40
30
20
10
0
C
Ip-10
**
***
**
600
400
200
D
Sting1
*
8
6
4
2
NF-κB dependent
E
Tnfα
30
F
Il-1β
200
150
100
50
G
Casp1
300
STING WT
STING ki

Figure 4.

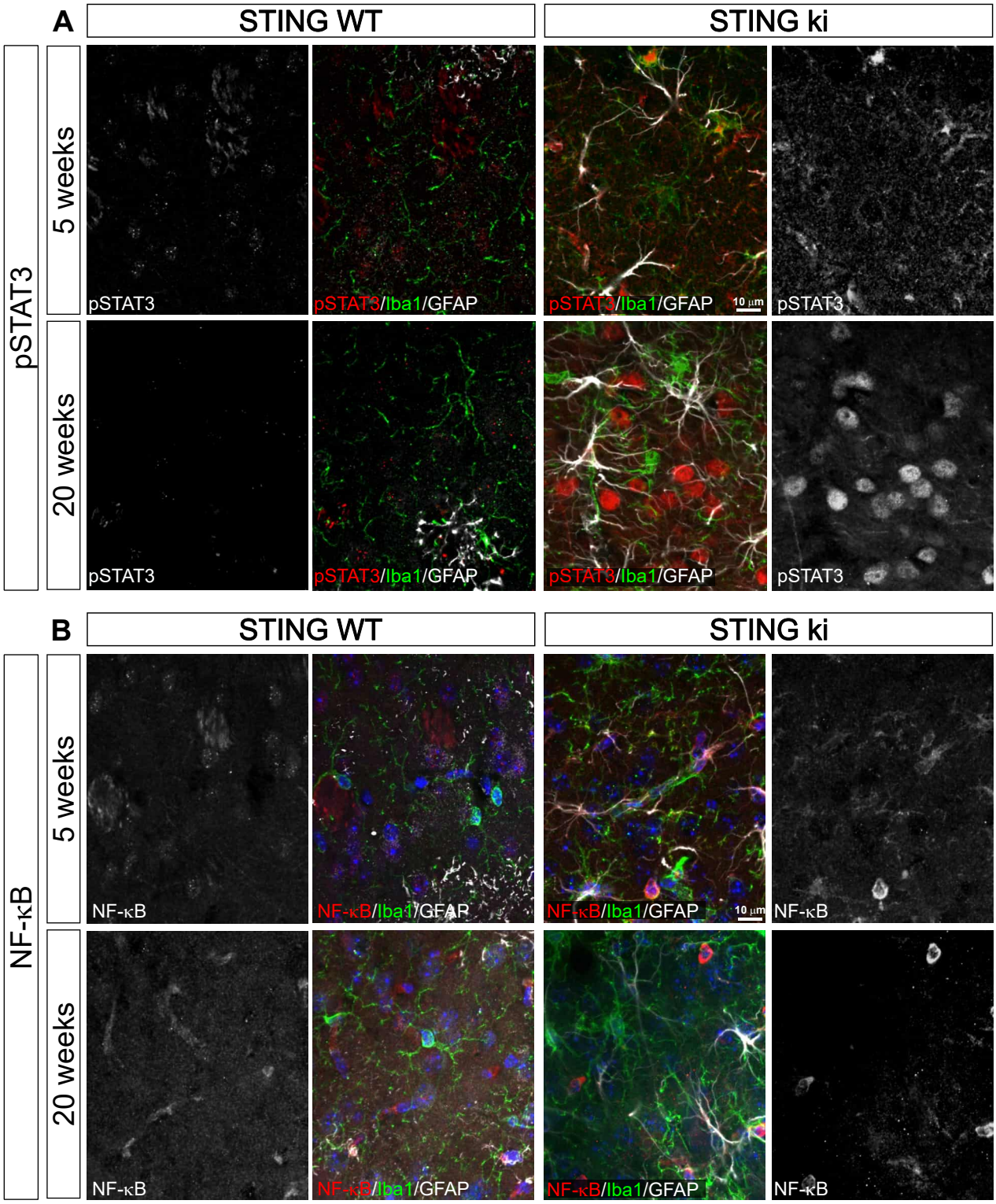
A
STING WT
STING ki
pSTAT3
5 weeks
20 weeks
pSTAT3
pSTAT3/Iba1/GFAP
10 µm
B
NF-κB
NF-κB/Iba1/GFAP

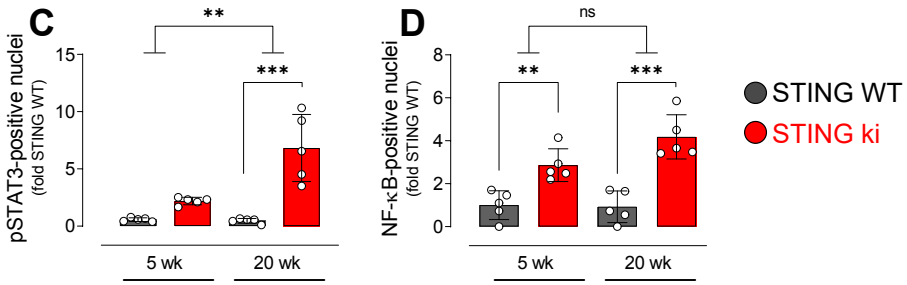
C
pSTAT3-positive nuclei
(fold STING WT)
15
10
5
0
**
***
5 wk
20 wk
D
NF-κB-positive nuclei
(fold STING WT)
8
6
4
2
0
ns
**
***
5 wk
20 wk
STING WT
STING ki

Figure 5.

Figure 6.

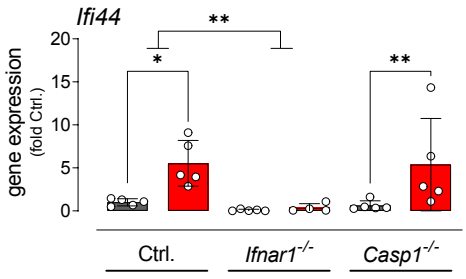

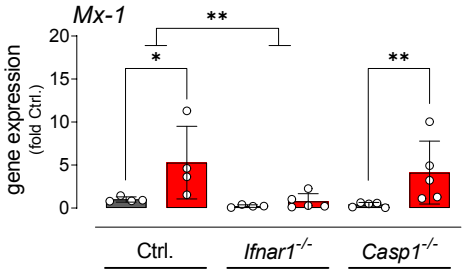

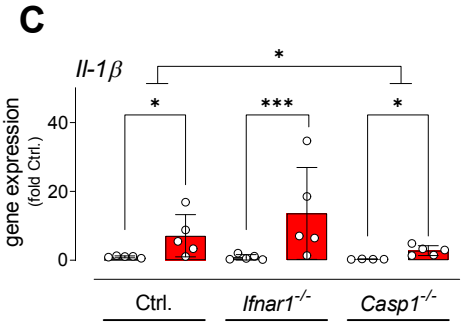

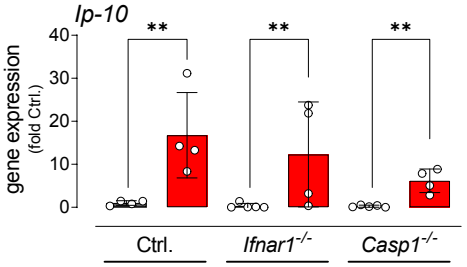

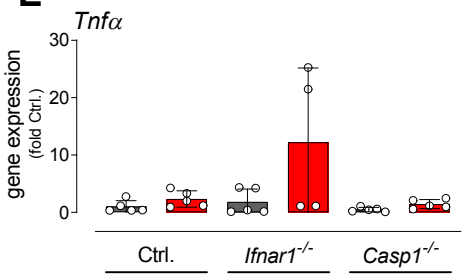

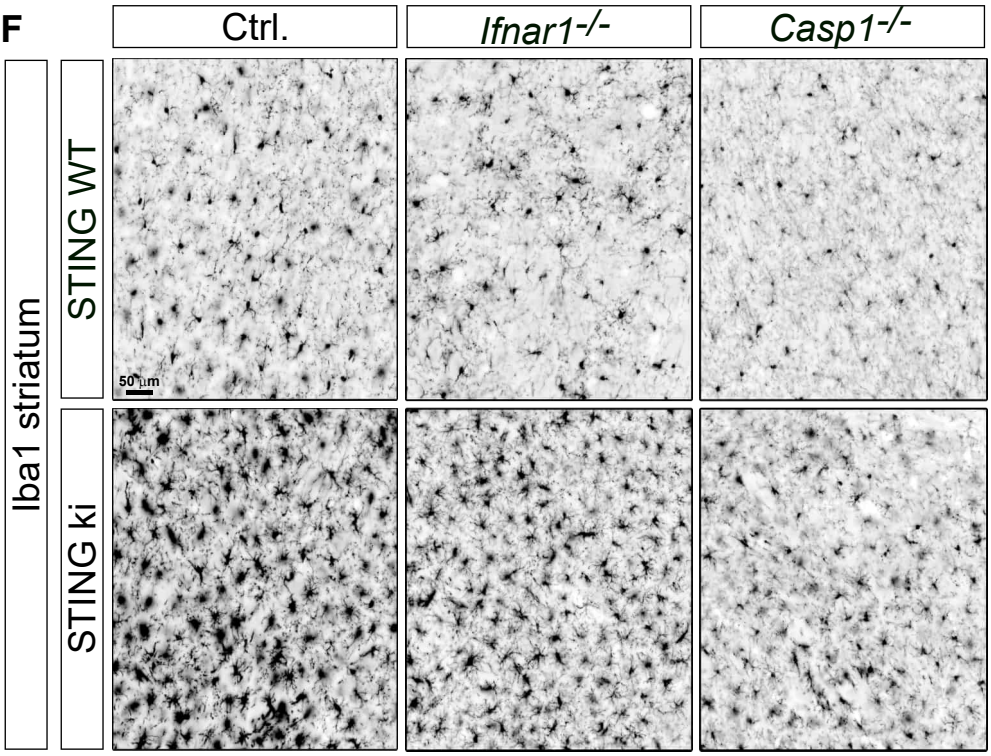

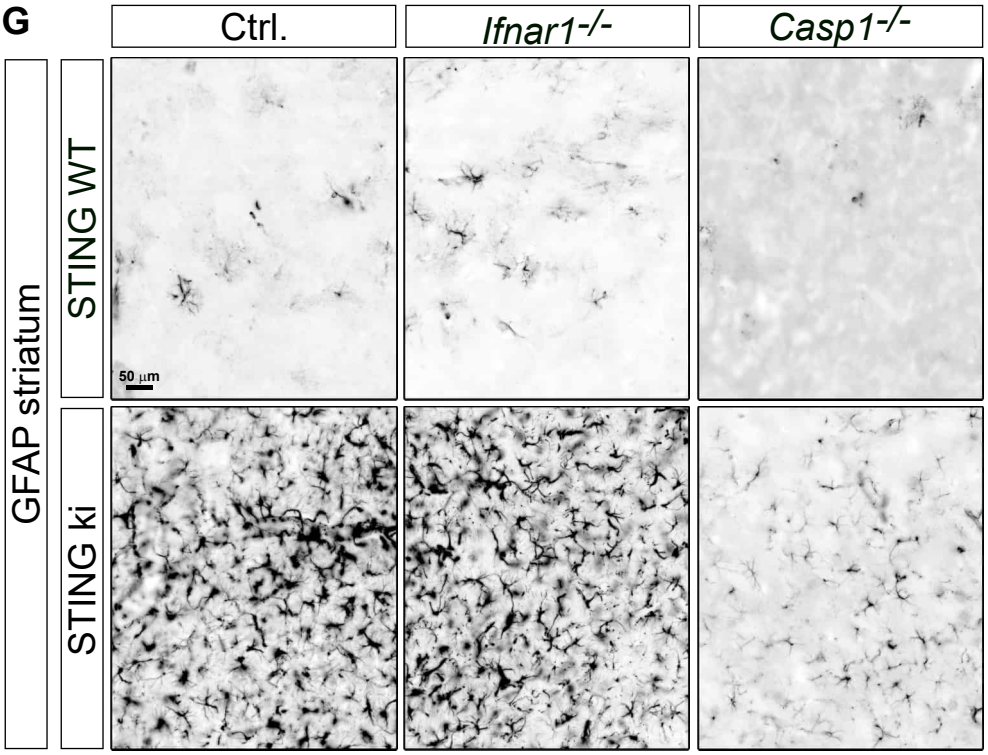

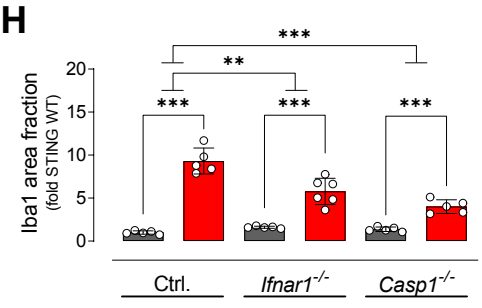

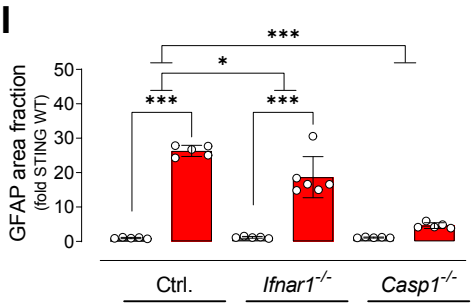

STING WT STING ki

Figure 7.

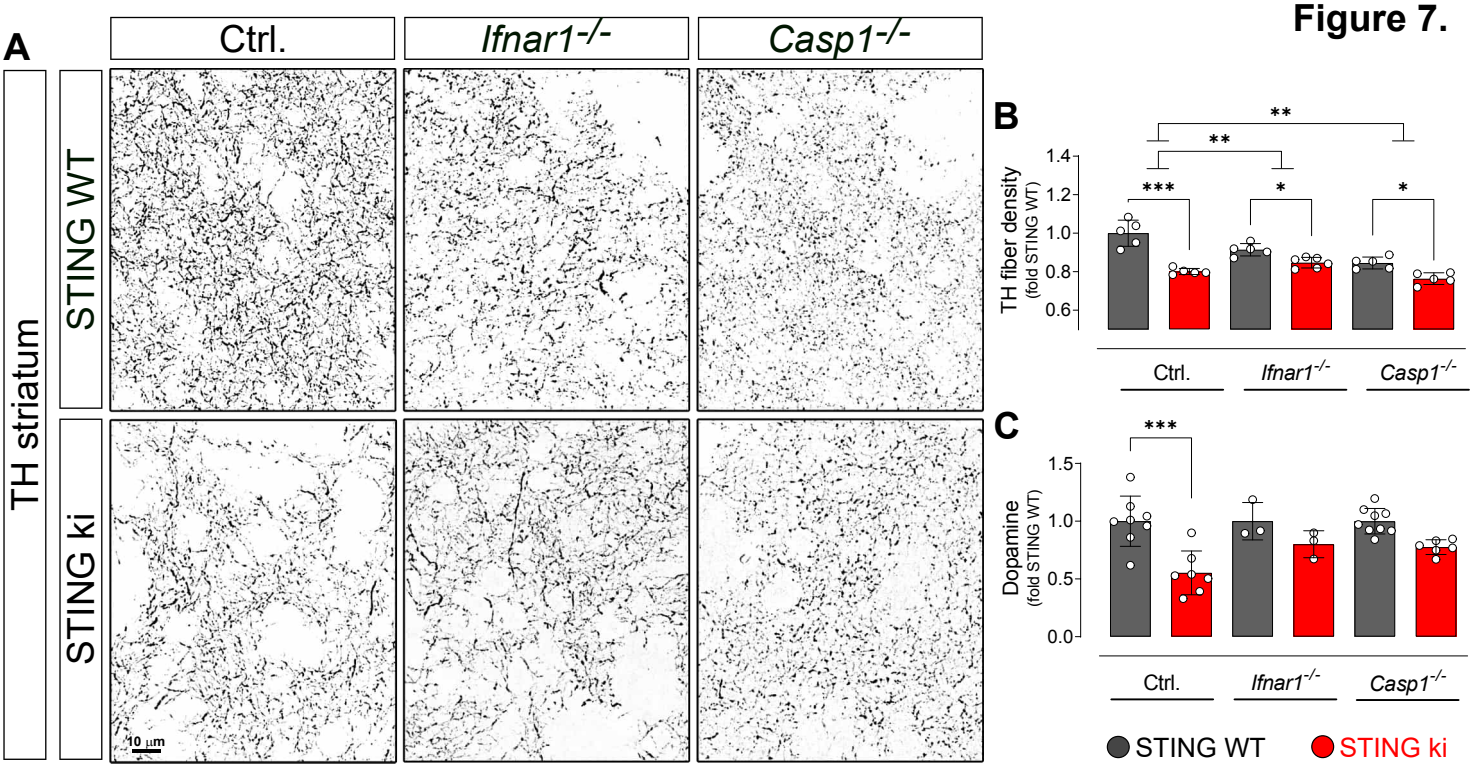
A
Ctrl.
Ifnar1-/-
Casp1-/-
TH striatum
STING WT
STING ki
10 µm
B
TH fiber density
(fold STING WT)
1.4
1.2
1.0
0.8
0.6
***
**
*
**
*
Ctrl.
Ifnar1-/-
Casp1-/-
C
Dopamine
(fold STING WT)
1.5
1.0
0.5
0.0
***
Ctrl.
Ifnar1-/-
Casp1-/-
STING WT
STING ki

Supplemental Figure 1

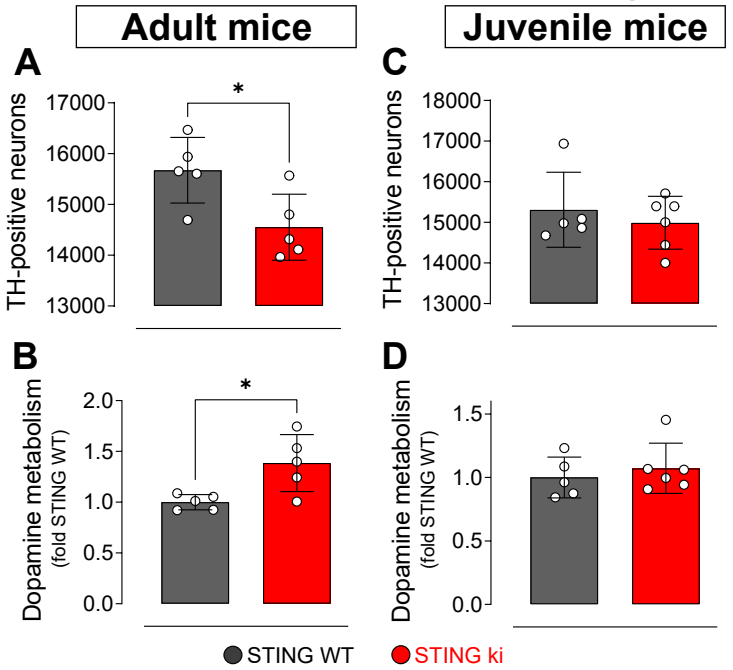
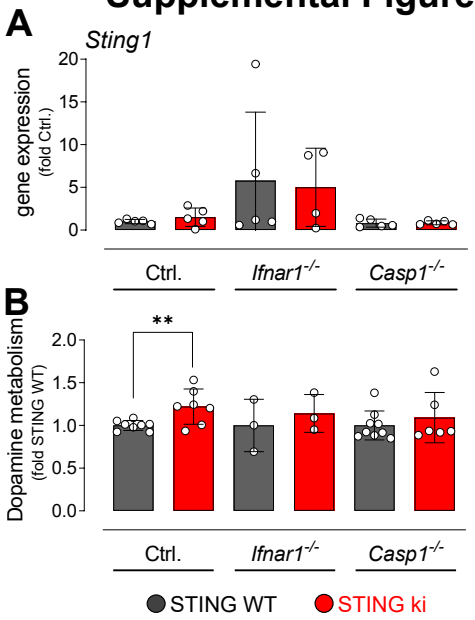
Supplemental Figure 2